מכון ויצמן למדע
WEIZMANN INSTITUTE OF SCIENCE

Thesis for the degree
Master of Science

עבודת גמר (תזה) לתואר
מוסמך למדעים

Submitted to the Scientific Council of the
Weizmann Institute of Science
Rehovot, Israel

מוגשת למועצה המדעית של
מכון ויצמן למדע
רחובות, ישראל

By
Meirav Pinkas

מאת
מירב פנקס

הדינמיקה של התפלגות האנרגיה של יון הלכוד בתוך ענן של אטומים קרים

Energy distribution dynamics of a trapped ion immersed in a cold cloud of atoms

Advisor: Prof. Roee Ozeri

מנחה: פרופ' רועי עוזרי

February 2018

אדר התשע"ח

Abstract

Hybrid systems that involve interactions between ultra-cold atoms and cold ions are a promising framework to study the quantum nature of atom-ion collisions at low temperatures. It can also serve as a new platform for quantum computation and many-body quantum simulation. However, many of these applications are currently unachievable since the interaction energy is limited to a few mK, even though both atoms and ions can be cooled down to a few μK. Heating arises from the fact that the atom-ion collisions occur in oscillating electric fields of the ion Paul trap, that on average, couple energy to the system. The fundamental limit of this effect emerges from the attracting $-\frac{1}{r^4}$ potential between the ion and the atom. This work investigates how the heating depends on different parameters, by using both a molecular dynamics simulation and an experiment with an $^{88}Sr^+ -^{87}Rb$ system.

The molecular dynamics simulation was used to find the heating rates and the dynamics of the ion energy distribution revealing a transition from a thermal cold distribution to a hotter non-thermal one with a high energy power-law tail. This behavior depends on various trap parameters and atom-ion mass ratio.

In the experiment, a ground-state-cooled $^{88}Sr^+$ ion was immersed in an ultra-cold cloud of ^{87}Rb atoms. The temperature of the ion was measured using Rabi carrier spectroscopy after different interaction times with the atomic cloud. This measurement was repeated for different axial and rf confinements of the Paul trap. No statistically significant difference in heating was observed when changing the axial confinement. However, the experiments revealed a slightly higher heating rate for a lower rf confinement whereas the prediction of the molecular dynamics simulation was opposite. This can be attributed to the ability to compensate stray static electric fields on the ion at different trap parameters.

Acknowledgments

First I would like to thank my supervisor Prof. Roee Ozeri, for encouraging me since the first day and introducing me the wonderful world of experimental quantum physics.

I am deeply grateful to Ziv Meir who welcomed me to the lab and always had the time and patience to explain and make things seem simple. The experiments could not be performed without the endless help of Ruti Ben-Shlomi and Tomas Sikorsky who helped me cope with all the problems that occurred.

I also want to thank the my fellow lab members Ravid Shaniv, Tom Manovitz, Yotam Shapira, Lee Peleg, Jonatan Piasetzky, Nitzan Akerman and Meir Alon who were always there to help and give valuable advice.

Last but not least, I would like to thank Yan for keeping me sane and for his infinite support.

Contents

1 Introduction

Performing experiments at low-temperatures can reveal the quantum nature of atoms and molecules. Laser-cooled ions and atoms were investigated separately during the last few decades. Trapped cold ions are a highly controllable system that can be used for the realizations of quantum computation processes[1] and precision measurements[2]. Trapped atoms can be cooled to their quantum ground state[3] and can be used to simulate many-body quantum systems[4].

Co-trapping ultra-cold atoms and cold ions offers new possibilities for exploring low-temperature collisions, that include phenomena such as s-wave scattering, Feshbach resonances[5], shape-resonances[6] and the creation of molecular ions[7]. In addition, it is also a promising platform for performing quantum computations[8] and quantum simulations[9].

In the last two decades, hybrid systems involving cold atoms and ions, were realized in many different experiments. Interaction was made both with ultra-cold thermal clouds and degenerate gases. Nonetheless, all these experiments were limited to atom-ion interaction energy of the mK regime. This energy scale is far greater than the energy scale of the quantum phenomena mentioned above.

This energy limit arises from the fact that in all experiments the ion is trapped using a Paul trap[10]. In Paul traps, the ion is confined by oscillating electric fields. Since the trapping potential is time-dependent, it is not conserving and can inject energy into the system. In 1968, it was observed by Major and Dehmelt[11] that ions in a Paul trap that collide with heavy atoms lead to exponential heating and therefore to ion loss. 40 years later DeVoe [12] numerically demonstrated that a single collision cannot cause this enormous heating effect, but a sequence of collisions which occurs at a certain phase of the trapping potential. He also showed that these consecutive collisions lead to a power-law energy distribution and not thermal, as expected in a thermalization process. This power-law tail of the distribution depends on the mass ratio between the atom and the ion. The Tsallis distribution was proposed to describe the result. Tsallis[13] originally proposed it as a generalization of thermal distribution in non-extensive statistical mechanics. Only recently was it shown, that this behavior arises from collision dynamics with atoms at a finite temperature[14].This distribution also depends on the specific Paul trap parameters.[15, 16]

In DeVoe's analysis, even though the ion can obtain substantial amount of energy, this energy can be lost immediately if a collision occurs at the center of the trap. As a result, in the steady state, the typical energy of the ion will be at the same scale as the energy of the atoms. This means that atoms at zero temperature would lead to an ion at zero temperature. However, in a later experiment[17] it was shown that the mean energy of the ion can be higher by orders of magnitude, than the energy of the atoms (for a specific mass ratio). This additional energy-scale arises from the fact that static electric fields can move the equilibrium position in such a way, that it will experience non vanishing rf fields (excess micromotion). Furthermore, the power-law exponent of the steady-state distribution depends, not only on the mass ratio, but also on the geometry of the Paul trap[18].

Due to imperfections in a realistic Paul trap, the ion, at its equilibrium position, will always experience some non vanishing rf fields. However, this effect can be compensated by applying an external static electric field that moves the ion to the null point of the rf field.[19] Even after a full compensation and an initial ion in its ground state, the first collision can get significantly higher energy than the temperature of the atoms as shown by Cetina et al[20]. This effect occurs due to the attractive polarization potential between the ion and the atoms that can cause the first collision to happen far from the equilibrium position of the ion - hence at a region with non vanishing electric fields. The same heating effect was observed experimentally by Meir et al. [21], where the trap was fully compensated and a ground state ion collided with ultra-cold atoms. In the last experiment, deviation from a thermal distribution was observed in the steady state.

This polarization potential induced heating was studied for the first collision but its effect on the energy distribution dynamics and steady-state is still unknown. In addition, this dynamics was not observed experimentally for different parameters of the Paul trap. This work investigates both questions using numerical tools and experimentally.

1.1 Atom-ion elastic collisions

1.1.1 Classical description

In the presence of the electric field created by the ion, the atom is polarized. The electric dipole of the atom is $p\left(r\right)=\alpha E\left(r\right)$ where α is the polarizability of the atom and $E\left(r\right)=\frac{e}{4\pi\epsilon_0 r^2}\hat{r}$ is the electric field created by the ion. The interaction energy is:

$$V\left(r\right)=-\frac{p\cdot E}{2}=-\frac{\alpha}{2}E^2=-\frac{\alpha e^2}{2\left(4\pi\epsilon_0\right)^2}\frac{1}{r^4}\equiv-\frac{C_4}{2r^2}$$

Where $C_4=\frac{\alpha e^2}{\left(4\pi\epsilon_0\right)^2}=1.09\cdot10^{-56}\ J\cdot m^4$ for $\alpha_{Rb}=h\cdot0.0794\ \frac{Hz}{\left(\frac{V}{cm}\right)^2}$[22].

The Hamiltonian for ion-atom interaction is:

$$H = \frac{p_{ion}^2}{2m_{ion}} + \frac{p_{atom}^2}{2m_{atom}} + V\left(|r_{ion} - r_{atom}|\right)$$

After preforming a change of variables to the center of mass position $R = \frac{m_{atom}r_{atom}+m_{ion}r_{ion}}{m_{atom}+m_{ion}}$ and the relative position $r = r_{ion} - r_{atom}$, the relative motion part is reduced to Hamiltonian of a single particle in a central potential:

$$H_{relative} = \frac{p^2}{2\mu} - \frac{C_4}{2r^4} \tag{1}$$

where $\frac{1}{\mu} = \frac{1}{m_{ion}} + \frac{1}{m_{atom}}$ is the reduced mass. This Hamiltonian has a characteristic length scale at which the kinetic energy of the center of mass is comparable to the polarization potential:

$$r_L = \sqrt[4]{\frac{2C_4}{E}}$$

The impact parameter of the collision:

$$b = \frac{|r \times p|}{p} = \frac{L}{\sqrt{2\mu E}}$$

Where $L = r \times p$ is the angular momentum and E is the energy of the collision. Since the potential is centrally symmetric, the angular momentum of the system is conserved. Writing the Hamiltonian in polar coordinates:

$$H = \frac{p_r^2}{2\mu} + \frac{L^2}{2\mu r^2} - \frac{C_4}{2r^4} \equiv \frac{p_r^2}{2\mu} + U_{eff}\left(r\right)$$

From energy conservation we can get that the minimal atom-ion distance is:

$$r_{min} = \sqrt{E\left(b^2 \pm \sqrt{b^4 - \frac{2C_4}{E}}\right)}$$

Where E is the collision energy. In order to get a real solution the impact parameter must satisfy $b > \sqrt[4]{\frac{2C_4}{E}} \equiv b_c$. Then collisions with impact parameter $b < b_c$ will terminate in a spiraling collision - also called *Langevin collision.* These collisions can transfer high momentum and cause inelastic processes

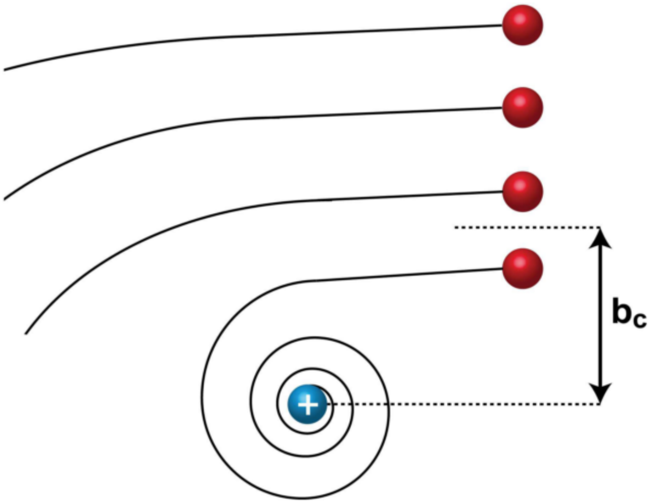

Figure 1: Two different types of atom-ion collisions. Collisions with an impact parameter larger than b_c can transfer only a small amount of energy and momentum that ends in a small deflection of the atoms. These collisions are called glancing collisions. Collisions with impact parameter smaller than b_c will cause head-on collision which can cause large energy and momentum change of the ion. These collisions are called Langevin collisions or hard-sphere collisions. Langevin collisions can also involve inelastic process such as charge-exchange or spin-exchange. The picture is taken from [23].

such as spin exchange, spin relaxation and charge exchange. Collisions with $b > b_c$ do not terminate with a close contact and can only transfer small momentum, these collisions also called *glancing collisions*.[1]

The cross section of the Langevin collisions is $\sigma_L = \pi b_c^2 \sim \frac{1}{\sqrt{E}}$ [24] and hence the Langevin collision rate is energy independent:

$$\Gamma_L = n_{atoms} v \sigma_L = n_{atoms} \pi \sqrt{\frac{4C_4}{\mu}}$$

1.1.2 s-wave limit

The effective 1D potential (1) has an angular momentum potential barrier at $r = \sqrt{\frac{2\mu C_4}{L^2}}$ with height $E = \frac{L^4}{8\mu C_4}$. The energy can be expressed by the angular momentum quantum number $\left(L^2 = l\left(l+1\right)\hbar\right)$:

---

[1] There are no close orbits for $\sim \frac{1}{r^4}$ potential. According to Bertrand's theorem closed orbits for centrally symmetric potential can only occur for $\sim \frac{1}{r}$ and $\sim \frac{1}{r^2}$ potentials.

$$E = \frac{l^2 \left(l+1\right)^2 \hbar^4}{8\mu^2 C_4}$$

S-wave scattering involves only a single partial wave with $l = 0$. The energy limit of this process is given by the potential barrier of $l = 1$ partial wave:

$$E < E_s = \frac{\hbar^4}{2\mu^2 C_4}$$

For $Sr^+ - Rb$ system, $E_s \simeq 80nK$. For $E \gg E_s$ regime the classical model of Langevin collision can be used.

1.2 Paul trap

Electric potential created by a static electric field satisfies Laplace equation, and hence has no local minima or maxima (due to the maximum principle). This means that, charged particle cannot be trapped using only a static electric a field. One way to overcome this problem is to add a magnetic field, as in a Penning trap. Another way, which is also used in our experiment, adding spatially-varyingusing MLE oscillating electric fields as in a Paul trap.

In Paul traps, the electric field in the center of the trap is approximately a quadruple field. In a linear Paul trap, the oscillating electric field creates confinement in the x-y plane and a static electric field creates a confinement in the z direction.

Applying an oscillating voltage (radio-frequency - RF) with frequency Ω and amplitude V_{RF} on the red electrodes (“RF”) gives an approximate quadruple potential in the center of the trap:

$$\Phi_{RF}\left(x,y,z,t\right) = \frac{V_{RF}}{2}\left(1 + \frac{x^2 - y^2}{R_0^2}\right)\cos\left(\Omega t\right)$$

Where Ω is the rf frequency and R_0 is a constant arising from the geometry of the electrodes.

In order to create a confinement in the z direction, a static DC voltage is applied to the green electrodes (“DC”) which create the static potential:

$$\Phi_{DC}\left(x,y,z,t\right) = \frac{V_{DC}}{Z_0^2}\left(z^2 - \frac{x^2 + y^2}{2}\right)$$

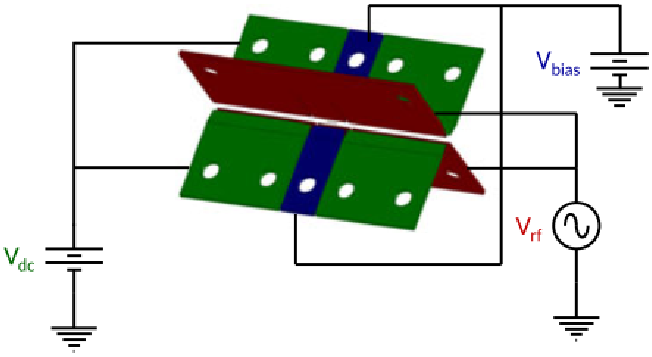

Figure 2: **Paul trap.** Linear segmented Paul trap which was used in the experiment to trap the ion. The RF electrodes (red) are driven at $\Omega = 2\pi \cdot 26.5 MHz$ at different voltages (600-900V in the experiment). The DC electrodes (green) was scanned across 250-600V. A bias dc voltage is applied to the blue electrodes in order to remove the degeneracy of the radial modes. Figure is taken from [25].

In this configuration the trapping potential is cylindrically symmetric. In order to break this symmetry [2] we apply a constant voltage on the blue electrodes ("BIAS"):

$$\Phi_{BIAS}(x, y, z, t) = \frac{V_{BIAS}}{2}\left(1 - \frac{x^2 - y^2}{R_0^2}\right)$$

The equations of motion are given by $(i = x, y, z)$:

$$\ddot{u}_i = -\frac{e}{m}\frac{\partial \Phi}{\partial u_i}$$

where e is the electron charge and m is the Sr^+ ion mass.

The last equation can be written as:

$$\ddot{u}_i + \frac{\Omega^2}{4}\left(a_i + 2q_i^2 \cos(\Omega t)\right) u_i = 0 \tag{2}$$

where:

---

[2] This is important in order to have an efficient single beam laser cooling.

$$a_{x,y} = -\frac{4e}{m\Omega^2}\left(\frac{V_{DC}}{Z_0^2} \mp \frac{V_{BIAS}}{R_0^2}\right) \qquad a_z = \frac{8e}{m\Omega^2}\frac{V_{DC}}{Z_0^2}$$

$$q_x = -q_y = \frac{2e}{m\Omega^2}\frac{V_{RF}}{R_0^2} \qquad q_z = 0$$

Equation (2) is also known as *Mathieu equation.* This equation can be solved using the Floquet theorem[26]. In the regime of $|a_i|, q_i^2 \ll 1$ (which is satisfied for most experimental realizations), the solution can be written in the lowest order as:

$$u_i(t) \approx A_i \cos(\omega_i t + \phi)\left[1 + \frac{q_i}{2}\cos(\Omega t)\right] \tag{3}$$

with:

$$\omega_i \approx \frac{\Omega}{2}\sqrt{a_i + \frac{q_i^2}{2}}$$

The trajectory can be decomposed into two motions with different timescales. The first is a *secular motion* with a low frequency ω_i:

$$u_i^{sec}(t) = A_i \cos(\omega_i t + \phi)$$

and the second is small and fast oscillatory motion - which is called *micromotion*:

$$u_i^{micromotion}(t) = u_i^{sec}(t)\,\frac{q_i}{2}\cos(\Omega t) \tag{4}$$

Since the potential is time-dependent, the instantaneous energy is not conserved. However, the energy is conserved after averaging over one secular motion cycle, to first order:

$$E_k \approx \frac{1}{4} m A_i^2 \left(\omega_i^2 + \frac{1}{8} q_i^2 \Omega^2\right)$$

We can see that the energy has two contributions, the first is the due to the secular harmonic motion, and the 2nd term is from the micromotion.

1.2.1 Excess micromotion (EMM)

In-phase excess micromotion Due to electrical imperfections of the trap, a uniform static electric field can be presented in the center of the trap. This will modify the equations of motion (2):[19]

$$\ddot{u}_i + \frac{\Omega^2}{4}\left(a_i + 2q_i^2 \cos\left(\Omega t\right)\right) u_i = \frac{e\boldsymbol{E}_{dc} \cdot \hat{u}_i}{m}$$

which adds to the solution a constant shift:

$$u_i\left(t\right) \approx \left(A_i^0 + A_i \cos\left(\omega_i t + \phi\right)\right)\left[1 + \frac{q_i}{2}\cos\left(\Omega t\right)\right]$$

Where $A_i^0 \approx \frac{e\boldsymbol{E}_{dc} \cdot \hat{u}_i}{m\omega_i^2}$. This gives additional micromotion $A_i^0 \frac{q_i}{2}\cos\left(\Omega t\right)$ which is called *in-phase excess micromotion*[3]. In contrast to *inherent mircomotion* as indicated in equation (4), this motion is not reduced when the secular motion of the ion is laser-cooled, and additional kinetic energy adds to the system:

$$E_k^{DC} = \frac{1}{4}m\left(\Omega A_i^0\right)^2 = \frac{1}{4m}\left(\frac{e\boldsymbol{E}_{dc} \cdot \hat{u}_i}{\omega_i^2}\frac{q_i \Omega}{2}\right)^2$$

This energy can be reduced by applying an external static electric field. The full procedure of detection and compensation of this EMM is described in (3.2.1).

Axial excess micromotion In addition to this stray constant electric field, there is a constant rf field on the axial axis of the trap. This can be also compensated by applying rf field with the same magnitude and opposite phase.

---

[3] An additional term oscillating in Ω out-of-phase can arise if there is a phase mismatch between the rf electrodes. If there is a phase mismatch φ_{ac} between the electrodes, there is an additional field in the the center of the trap oscillating out of phase:

$$\boldsymbol{E} = -V_{RF} \sin\varphi_{ac} \sin\left(\Omega t\right) \boldsymbol{\beta}_{RF}$$

Where $\boldsymbol{\beta}_{RF}$ is the electric field in the center of the trap created by 1V on the rf electrodes. However, in our system, this effect is much smaller than the EMM after compensation and hence does not apparent in the dynamics.

1.3 Collisions in a Paul trap

When a hot system comes in contact with a cold bath, it will thermalize to the temperature of the bath. This process is known as *sympathetic cooling.* The underlying mechanism is that when a fast (hot) particle collides with a slow (cold) particle, they exchange energy and the result is a net loss of energy of the hot particle. This cooling mechanism is most efficient for equal mass particles. Sympathetic cooling by ultra-cold atoms was proposed as a cooling mechanism for ions since atoms can be cooled by into lower temperatures than ions.

This mechanism fails to work in a Paul trap since the system is not closed, the oscillating electric fields can couple additional energy to the system. Already in 1968, Major and Dehmelt[11] showed that for trapped ions colliding with atoms the mean energy of the ions increases for $m_{atom} \gg m_{ion}$ and decreases for $m_{atom} \ll m_{ion}$. For $m_{atom} \approxeq m_{ion}$it was predicted to give zero change in the mean energy.

Consider an ion with mass m_i and velocity v_{ion} collides with an atom with mass m_a at rest. In the moment of the collision, the external RF field has amplitude E and phase ϕ. The velocity of the ion composed from the secular velocity and the micromotion velocity:

$$v_{ion} = -\omega A \sin(\omega t) + \frac{q\Omega}{2} A \sin(\omega t) \sin(\Omega t) \equiv v_{sec} + v_{mm}$$

In the center of mass (CM) frame:

$$v_{ion}^{CM} = v_{ion} - v_{cm}, \quad v_{atom} = -v_{cm}$$

where $v_{cm} = \frac{m_i v_{ion}}{m_i + m_a} = \beta v_{ion}$, $\beta = \frac{m_i}{m_a + m_i}$. Assume the scattering angle is given by the rotation matrix $\mathcal{R}$ in the center of mass frame relative to v_{ion} direction.

$$v_{ion}^{\prime CM} = \mathcal{R} v_{ion}^{CM} = \mathcal{R}(v_{ion} - v_{cm}) = (1-\beta)\mathcal{R} v_{ion}$$

The velocity of the ion after the collision in the lab frame:

$$\begin{aligned} v'_{ion} &= (1-\beta)\mathcal{R} v_{ion} + v_{cm} \\ &= (1-\beta)\mathcal{R} v_{ion} + \beta v_{ion} \end{aligned}$$

The micromotion velocity is unaffected by the collision[4], means: $v'_{ion} = v'_{sec} + v_{mm}$

$$v'_{sec} + v_{mm} = (1-\beta)\,\mathcal{R}\,(v_{sec} + v_{mm}) + \beta\,(v_{sec} + v_{mm})$$

$$v'_{sec} = (1-\beta)\,\mathcal{R}v_{sec} + \beta v_{sec} + (1-\beta)\,(\mathcal{R}-1)\,v_{mm} \tag{5}$$

To see the effect of collision in presence on micromotion, we can take the simple case of collision in 1D with $\mathcal{R} = -1$:

$$\begin{aligned} v'_{sec} &= -\,(1-\beta)\,v_{sec} + \beta v_{sec} - 2\,(1-\beta)\,v_{mm} \\ &= (2\beta-1)\,v_{sec} - 2\,(1-\beta)\,v_{mm} \end{aligned} \tag{6}$$

The micromotion velocity at each time can be written as function of the secular velocity:

$$v_{mm} = -\frac{q\Omega}{2\omega}\sin(\Omega t)\,v_{sec}$$

Then, the secular velocity after a collision:

$$v'_{sec} = \left[(2\beta-1) + 2\,(1-\beta)\,\frac{q\Omega}{2\omega}\sin(\Omega t)\right] v_{sec}$$

This expression shows that the micromotion energy can couple into the secular energy of the ion and hence can increase (or decrease) its temperature. In the limit of heavy ion ($\beta \to 1$) the micromotion term vanishes, whereas in the light ion limit ($\beta \to 0$) we get the maximal contribution of micromotion. For equal mass particles (as in a $Sr^+ - Rb$ collision), $\beta = \frac{1}{2}$ and we get $v'_{sec} = -v_{mm}$. For the same mass ratio in free particles collision we would get an entire loss of the ion's energy.

Generalizing the last expression to many collisions give that the velocity after N collisions is given by:

$$v_{sec}^{N} = \omega A_0 \sin(\omega t)\,\Pi_{i=0}^{N}\left[(2\beta-1) + 2\,(1-\beta)\,\frac{q\Omega}{2\omega}\sin(\Omega t_i)\right]\sin(\omega t_i)$$

---

[4] For excess micromotion, the inherent micromotion is proportional to the secular amplitude.

Where t_i are the collision times and A_0 is the initial amplitude.

We can see that the amplitude, and hence the energy, can be represented as a multiplication of random variables. As opposed to the sum of independent and identically distributed random variables which converges to a Gaussian distribution, multiplication of random variables can give a rise to a power law distribution. In addition, the mean value of these distributions is dominated by a few rare events.[27]

A generalization of Maxwell-Boltzmann distribution with a high-energy power law is the *Tsallis distribution*[13]:

$$P\left(E\right)=\frac{\left(n-3\right)\left(n-2\right)\left(n-1\right)}{2\left(nk_BT\right)^3}\frac{E^2}{\left(1+\frac{E}{nk_BT}\right)^n} \tag{7}$$

Where T describes the energy scale of the distribution whereas n describes the power-law of the high energies tail (for large E, $P\left(E\right)\propto E^{2-n}$).

Note that for $n\to\infty$ we get the usual thermal distribution:

$$P_{n\to\infty}\left(E\right)=2\sqrt{\frac{E}{\pi}}\left(\frac{1}{k_BT}\right)^{3/2}e^{-\frac{E}{k_BT}} \tag{8}$$

Since this distribution has two parameters, a “temperature” cannot be defined. In addition, this distribution has a diverging mean for $n\leq 4$ and hence the distribution cannot be described by its mean. However, the most probable energy include both parameters of the distribution (the energy scale T and the power-law n):

$$k_BT_{ion}\equiv k_BT\frac{n}{n-2}=\frac{E_{mode}}{2}$$

Note that this temperature converges to the thermal temperature at the limit of thermal distribution ($n\to\infty$).

This distribution was shown to arise from consecutive collisions in the presence of micromotion and atoms at non-zero temperatures [14].

1.4 Atom-photon interaction

This section mainly follows Leibfried et al. review[26]. A two level system can be described by the Hamiltonian:

$$\mathcal{H}_e = \hbar\frac{\omega_0}{2}\left(|e\rangle\langle e| - |g\rangle\langle g|\right) \equiv \hbar\frac{\omega_0}{2}\sigma_z$$

Where $|g\rangle$ and $|e\rangle$ are the ground and excited states respectivly and $\omega_0 = \omega_e - \omega_g$ is the energy difference between the levels. In our case, $|g\rangle$ and $|e\rangle$ are different electronic states of the Sr^+ion.

The harmonic potential of the Paul trap is described by a motional part:[5]

$$\mathcal{H}_m = \frac{p_i^2}{2m} + \frac{m}{2}\nu_i^2 x_i^2$$

Where i is the index of the different motional modes and ν_i are the secular frequencies.

The interactions between the laser field and two level system (in our case, the Sr^+ ion) are described by the Hamiltonian:

$$\mathcal{H}_i = \frac{\hbar}{2}\Omega\left(|g\rangle\langle e| + |e\rangle\langle g|\right)\left[e^{i(\boldsymbol{k}\cdot\hat{x} - \omega t + \phi)} + e^{-i(\boldsymbol{k}\cdot\hat{x} - \omega t + \phi)}\right]$$

Where Ω is the on-resonance Rabi frequency (coupling of the light field to the electronic transition), $\hat{x}$ is the position of the ion, $\boldsymbol{k}$ is the direction of the laser beam, and ω is the laser frequency.

After moving to the interaction picture with the free Hamiltonian $\mathcal{H}_0 = \mathcal{H}_m + \mathcal{H}_e$, and preforming rotating wave approximation, the Hamiltonian reduces to:

$$\mathcal{H}_i = \frac{\hbar}{2}\Omega_0\hat{\sigma}_+ \exp\left\{ i\sum_j \eta_j\left(\hat{a}_j e^{-i\nu t} + \hat{a}_j^\dagger e^{i\nu t}\right)\right\} e^{i(\phi - \delta t)} + H.c.$$

Where $\Omega_0 = \frac{\Omega}{\Pi_j\left(1+\frac{q_j}{2}\right)}$ is the modified Rabi frequency due to the micromotion of the ion, $\eta_i = k_i x_{0,i} = k_i\sqrt{\frac{\hbar}{2m\nu_i}}$ is the Lamb-Dicke parameter, $\delta = \omega - \omega_0$ is the detuning from the atomic resonance frequency ω_0, a_j and $a_j^\dagger$ are the creation and annihilation operators of the i-th mode of the harmonic oscillator and:

$$\hat{\sigma}_+ = \frac{1}{2}\left(\hat{\sigma}_x + i\hat{\sigma}_y\right) = \frac{1}{2}\left[\left(|e\rangle\langle g| + |g\rangle\langle e|\right) - \left(|g\rangle\langle e| - |e\rangle\langle g|\right)\right] = |e\rangle\langle g|$$

When the system is in the Lamb-Dicke regime ($\eta \ll 1$) this Hamiltonian can be approximate to:

---

[5] The time dependent part of the frequency (due to micromotion) is not taken into account here.

$$\mathcal{H}_i^{LD} = \frac{\hbar}{2}\Omega_0\hat{\sigma}_+ \left(1 + i\sum_j \eta_j \left(\hat{a}_j e^{-i\nu t} + \hat{a}_j^\dagger e^{i\nu t}\right)\right) e^{i(\phi-\delta t)} + H.c.$$

An arbitrary state can be written by:

$$|\Psi\left(t\right)\rangle = \sum_{n=0}^{\infty}\left[c_{n,g}\left(t\right)|n,g\rangle + c_{n,e}\left(t\right)|n,e\rangle\right] \tag{9}$$

and its time evolution is given by the Schrödinger equation:

$$i\hbar\partial_t|\Psi\left(t\right)\rangle = \mathcal{H}_i^{LD}|\Psi\left(t\right)\rangle \tag{10}$$

By plugging equation (9) into equation (10) we can get coupled differential equations for the coefficients $c_{n,e}\left(t\right)$ and $c_{n,e}\left(t\right)$, and hence the probability to be at ground or exited stated at any given time.

2 Numerical simulation - Collisions with polarization potential

Assume that the EMM in the system is fully compensated in addition to the ground-state cooled ion and ultra-cold atoms. Will the ion now thermilize to the temperature of the atoms? Cetina et al.[20] showed that in this case even the first collision can heat the ion. The atom-ion potential displaces the ion from the center of the trap when the atom approaches and the collision occurs at non-zero RF fields which can inject or remove energy from the ion. This means that the assumption of the collision as instantaneous hard-sphere collision is not valid. The work done by the rf field in the first collision can be described by the energy scale[20]:

$$W_0 = 2\left(\frac{m_a}{m_i + m_a}\right)^{5/3}\left(\frac{m_i^2\omega^4 C_4}{q^2}\right)^{1/3} \tag{11}$$

As in the case of collisions with EMM, the gain or loss of energy depends on the phase of the rf field in which the collision occurs. This energy scale depends on the masses of the two particles. For our system $W_0 \approx 1.5mK$. By comparison, for $Li^+ - Yb$ system $W_0 \approx 13\mu K$. This means that the energy that is injected in a single collision is still much larger than the s-wave limit and a single vibrational energy quanta .

In order to investigate this effect further by numerical simulation, a different approach was taken. The collisions cannot be taken as instantaneous and the effect of the polarization potential must be taken into account by calculating the exact trajectory. In order to retrieve the energy distribution of the ion, the dynamics has to be calculated over many realizations of the system. In each realization, the ion starts in a thermal state with $T = 0.5mK$. The total energy is taken from a Maxwell-Boltzmann distribution and is divided equally between the three modes of the secular motion. In each mode, the amplitude in calculated by $A_i = \sqrt{\frac{2E_{mode}}{m\omega_i^2}}$ and the initial phase in taken from a uniform distribution in $[0, 2\pi]$.

In order to simplify the calculation and reduce the running time, we define an “interaction sphere” with radius $R_{interaction}$ around the center of the trap in which the full time evolution is evaluated. It was assumed that at each time there is only one atom in this interaction sphere.[6]

---

[6] The common atom density in the experiments was $n = 10^{17}m^{-3}$, which gives $\frac{4\pi}{3}R^3_{interaction}n \approx 0.7$ atoms inside the

The atoms are entering the sphere by rate $\Gamma_{atoms} = n\sigma v_{th}$ where n is the atoms density (Gasussian distribution), $\sigma = \pi R_{int}^2$ (cross section of a rigid sphere) and $v_{th} = \sqrt{\frac{8k_BT}{\pi m_a}}$ is the thermal velocity of the atoms (mean of the magnitude of the velocity in a thermal distribution). The interaction sphere radius must be larger than the amplitude of the ion motion. R_{int} initial value is taken to be $1.2\mu m$ which corresponds to ion energy of $\sim 1mK$. If the ion has a comparable amplitude to R_{int} after a collision, the interaction sphere radius is increased and remains at the same size until the end of this realization (the rate of the atoms is accordingly changed).

The position of atoms is distributed uniformly on the sphere. In order to generate a uniformly distribution unit vector, the azimuth angle φ is sampled from a uniform distribution on $[0, 2\pi]$ and the polar angle θ is sampled such that $\cos\theta$ is uniformly distribution in $[-1, 1]$.

The velocity amplitude is sampled from the following distribution using acceptance-rejection method:

$$p_T(v) = \frac{2m_{atom}}{(k_BT)^2} v^3 e^{-\frac{m_{atom}v^2}{2k_BT}}$$

the polar angle is sampled from the distribution $p(\theta) = \sin(2\theta)$ and φ from uniform distribution on $[0, 2\pi]$ as before. This will create a velocity assuming the atom position is at the south pole, hence the velocity vector is rotated to match the position of the atom.[7]

The majority of the atoms that enters this interaction sphere will not cause a hard-sphere collision and will barely change the ion energy. In order to reduce the demanding calculation of solving equations of motion, we check if the atom would come in proximity of the ion neglecting the polarization potential. We can define a characteristic length scale in which the harmonic potential and the interaction potential are equal:

$$\frac{1}{2}m_i\omega^2R_0^2 = \frac{C_4}{2R_0^4} \Rightarrow R_0 = \left(\frac{C_4}{\omega^2 m_i}\right)^{1/6}$$

For $Sr^+ - Rb$ system with typical values of $q = 0.1$ and $\omega = 1MHz$ this characteristic length-scale is $R_0 \approx 64nm$. This means that for $r \gg R_0$ the polarization potential can be neglected. The ion can

---

interaction sphere.

[7] There is an equivalent method to sample the velocity. The component which is parallel to the normal is taken from Rayleigh distribution with scale factor of $\sqrt{\frac{k_BT}{m_{atom}}}$ and the two other components taken from normal distribution with zero mean and $\sigma = \sqrt{\frac{k_BT}{m_{atom}}}$. This gives direction Maxwell-Boltzmann distribution.

be treated as a particle in a harmonic potential and the atom is a free particle, and hence moves in a straight line. A rough estimation of occurrence of a collision was done by calculating the minimal distance between the particles neglecting the polarization potential. If the minimal distance is much larger than R_0, the particles are not likely to collide and hence the trajectory is not calculated. This cut-off distance was chosen to be $100nm$, a bit larger than R_0 in order to ensure not to miss collisions.

If the particles are expected to collide, a full calculation of the trajectory is preformed by solving 12 coupled differential equations:[8]

$$\begin{aligned}
\dot{v}_{ion,i} &= -\frac{1}{m_{ion}}\frac{C_4\left(r_{ion,i}-r_{atom,i}\right)}{2\left|\boldsymbol{r}_{ion}-\boldsymbol{r}_{atom}\right|^5}-\frac{\Omega^2}{4}\left(a_i+2q_i\cos\left(\Omega t\right)\right)r_{ion,i} \qquad (12)\\
\dot{\boldsymbol{r}}_{ion} &= \boldsymbol{v}_{ion}\\
\dot{v}_{atom,i} &= \frac{1}{m_{atom}}\frac{C_4\left(r_{ion,i}-r_{atom,i}\right)}{2\left|\boldsymbol{r}_{ion}-\boldsymbol{r}_{atom}\right|^5}\\
\dot{\boldsymbol{r}}_{atom} &= \boldsymbol{v}_{atom}
\end{aligned}$$

These equations are solved using 4th order Runge-Kutta method. When the atom-ion distance is less than a critical distance of $5nm$, elastic hard sphere collision is assumed and the atom leaves at some random angle. Depending on the rf phase, a temporary bound state can be created as the atom has not enough energy to escape and collides a few more times until it gains enough energy. After a hard-sphere collision, equations (6) are solved until the the atom exits from the interaction sphere.

After this calculation is done, the ion is in position $u\left(t\right)$ with velocity $v\left(t\right)$. The ion's secular motion amplitude and phase can be calculated by (form equation (3)):

$$A_i\cos\left(\omega_i t+\phi_i\right)=\frac{u_i\left(t\right)}{\left[1+\frac{q_i}{2}\cos\left(\Omega t\right)\right]}$$

$$-A_i sin\left(\omega_i t+\phi_i\right)=\frac{v_i\left(t\right)}{\omega_i\left[1+\frac{q_i}{2}\cos\left(\Omega t\right)\right]}+\frac{\Omega\frac{q_i}{2}u_i\left(t\right)\sin\left(\Omega t\right)}{\omega_i\left[1+\frac{q_i}{2}\cos\left(\Omega t\right)\right]^2}$$

And then its (secular) energy in the i-th axis is given by: $E_i=\frac{1}{2}m\omega_i^2A_i^2$

Between each two atoms that enter the sphere, the motion of the ion is calculated by Eq. (3). This

---

[8] The EMM is not included in the equations, but it can be easily added to the first equation.

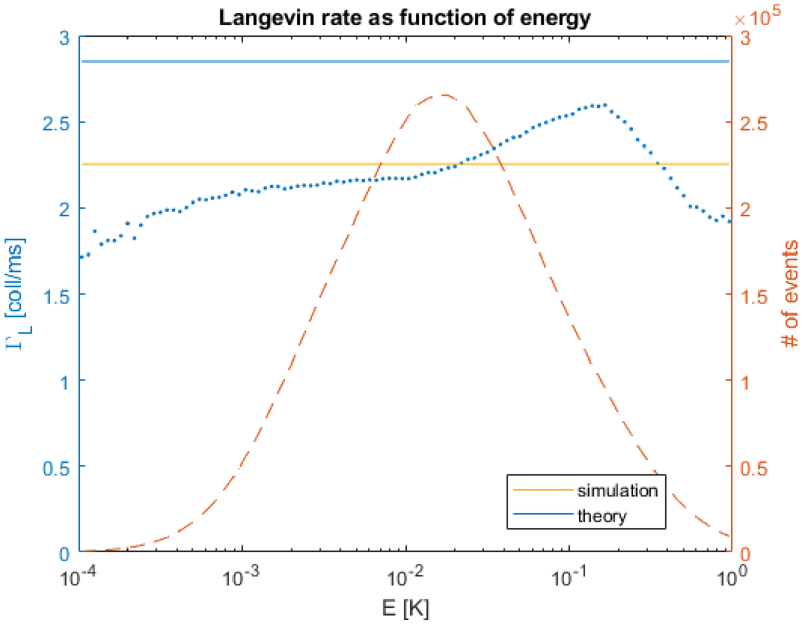

Figure 3: Langevin rate as function of energy. Blue dots - the mean time between to consecutive collision was calculated with logarithmic bins in the energy. Red dashed line - number of events in each bin. Yellow line - the Langevin rate as calculated from all time differences. Blue line - Langevin rate as calculated from the atomic density.

process is repeated until the running time exceeds the predefined experiment time. In order to get the energy distribution, many realizations with different initial conditions of the ion are calculated.

In this simulation, the Langevin collision rate (and its energy independence) is not taken as an assumption. The collision rate can be calculated from the simulation by binning the time difference between collisions as function of energy, see Fig. (3). The collision rate is weakly energy dependant, but it seems approximately constant, around the $1-100mK$ regime that contains the majority of collisions. In addition, the total Langevin rate is slightly lower than the expected rate (given by the input density of atoms). However, when calculating the rate, we normalized to the Langevin rate given by the simulation.

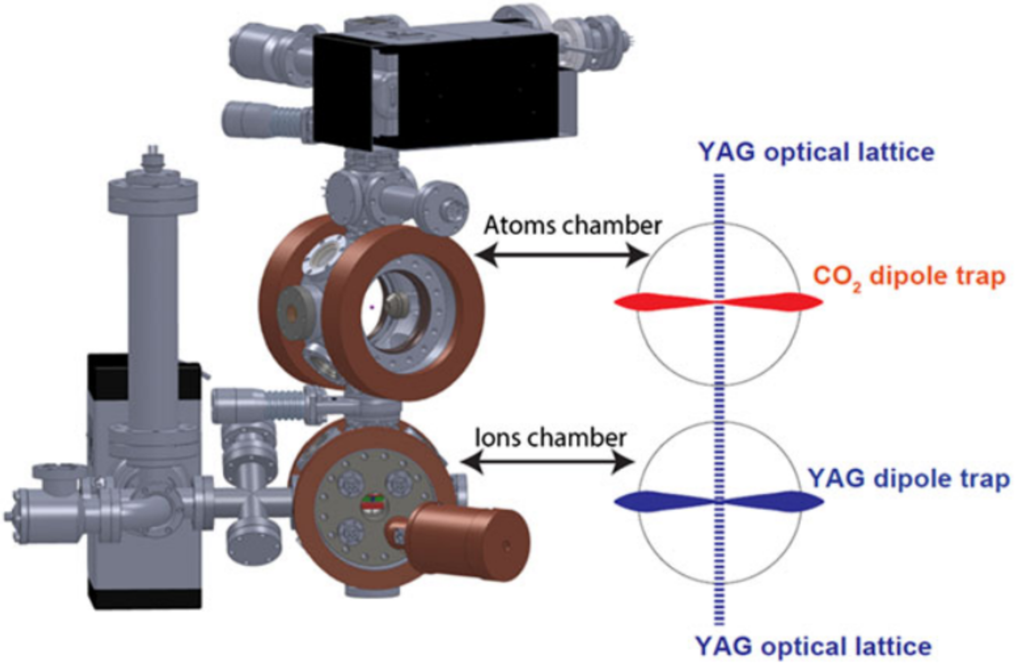

Figure 4: The atoms and ion vacuum chambers. Left - A SolidWorks drawing. Right - a scheme of the different atomic optical traps. The atoms are first collected and cooled in the upper chamber in a MOT (not shown) and then transferred to a CO_2 dipole trap for evaporative cooling. From the CO_2 trap they are loaded into two counter-propagating YAG beams which create 1D optical lattice. By changing the frequency of one of the beams, the lattice is moved to the lower chamber. In the lower chamber they are loaded into a cross-dipole trap created by a third YAG beam which can change its position to the ion position. Figure is taken from [25].

3 Experimental system

The experimental system is described in detail in refs. [25, 21]. Here, the main properties of the system, relevant to this work, will be reviewed.

3.1 Preparing the Rb atoms

The system consists of two vacuum chambers connected by a thin tube, see Fig. (4). In the upper chamber the atoms are trapped and cooled to a temperature of few μK. The ^{87}Rb atoms are loaded into a magneto-optical-trap (MOT) from an oven of isotope enriched source. The MOT contains six counter-propagating 780nm beams (18MHz detuned from the $F = 2 \rightarrow F' = 3$ transition) and a single repump beam ($F = 1 \rightarrow F' = 2$ transition). For the experiments in this work, the MOT loading time was a few seconds ending with 1-10 millions of atoms in the MOT. Then, the atoms are loaded into quasi-electrostatic trap formed by a CO_2 beam ($\lambda = 10.6\mu m$ $P = 15W$) tightly focused to a waist of $w = 30\mu m$ on the center of the MOT. In the CO_2 trap, evaporative cooling is done by ramping down the power of the laser. When decreasing power, the hottest atoms in the tail of the energy distribution are lost from the trap. This step ends with $\sim 10^4$ atoms at temperature of a few μK.

In order to move the atoms into the lower chamber, where the ion is trapped, the atoms are loaded into a 1D lattice created by 2 counter-propagating YAG laser beams ($\lambda = 1064nm,\ P = 5W$). By changing the relative frequency between the beams, the lattice moves and the atoms are transported into the lower chamber. The lattice stops when the atoms are $50\mu m$ above the ion position. In the vertical direction, the lattice sites have a width of $\frac{\lambda}{2} \approx 0.5\mu m$ compared with $10's\ \mu m$ in the horizontal direction. In order to create a more homogeneous atoms density distribution, the atoms are moved into a crossed dipole trap created by one of the the lattice beams and an additional beam ($w = 50\mu m,\ P = 1W$) which is focused on the ion. The additional beam position is controlled by a mirror mounted on a piezoelectric motor which causes the crossed dipole trap to move $50\mu m$ down to the ion position. This crossed-dipole trap creates a cloud of atoms with radius $\sim 5\mu m$ and length of $\sim 70\mu m$.

3.1.1 Atomic cloud size, density and temperature measurement

The collision dynamics depends on the density and the temperature of the atomic cloud. The atoms can be imaged in both chambers with absorption imaging.

From the Beer-Lambert law the attenuation of light going through a material (in the x direction) is given by:

$$I\left(x, y, z\right) = I_0 e^{-\sigma \int_{-\infty}^{x} n(x',y,z)dx'}$$

Where n is the local density of the particles, σ is the attenuation cross section and I is the measured intensity. Then, the number of atoms in a column at position (y, z) is given by:

$$\tilde{n}\left(y, z\right) \equiv \int_{-\infty}^{\infty} n\left(x'\right) dx' = -\frac{1}{\sigma} \log \frac{I_f}{I_0}$$

By measuring images with and without the atomic cloud, we can get the column density at each point. Integrating over the whole image gives the total number of atoms.

In each interaction experiment, the atoms are imaged in time-of-flight (TOF) method. When the dipole trap is turned off, the atomic cloud expands as:

$$\sigma_i\left(t\right) = \sigma_i^2\left(0\right) + \sigma_{v,i}^2 t^2 \tag{13}$$

where $\sigma_i\left(t\right)$is the width of the atomic cloud in i direction (fitted to Gaussian), σ_v is the "thermal size" of the could given by $\sigma_v = \sqrt{\frac{k_B T}{m}}$ and t is the time-of-flight. By measuring the size of the atomic cloud for different times of flight, we can get the temperature of the cloud and its original size. However, these parameters also depend on the length of the absorption beam pulse. In order to get the proper size and temperature, we repeat the TOF measurements for different pulse lengths. For each pulse, we fit the data to Eq. (13) to find σ_0 and dynamics T and then extrapolate to zero pulse length in order to find the "real" σ_0 and T.

3.2 Sr+ ion trapping, cooling and detection

The Sr^+ ion is created by two-photon ionization process (see Fig. 5 (a)). The first laser is tuned to the $5s^2\ {}^1S_0 \rightarrow 5s5p\ {}^1P_1$ transition at 461nm and the second one tuned to $5s5p\ {}^1P_1 \rightarrow\ {}^1D_2$ transition at 405nm. The ${}^1D_2$ level has linewidth of ~1nm and is an autoionizing level. The 461nm laser is generated by doubling a 922nm laser with a Toptica SHG module. The laser is locked to an atomic Sr cell using saturation-absorption method. The 405nm laser is generated by a bare photodiode. When the ion is ionized it is immediately trapped into the Paul trap. The trap is a segmented linear Paul trap (see Fig. 2 and discussion in section 1.2).

3.2.1 Minimization of excess micromotion

The EMM modulates the electric field of the laser beam in the rest frame of the ion[19]:

$$E_{laser}\left(t\right) = \Re\left[E_0 e^{i\left(\boldsymbol{k}\cdot\boldsymbol{u}_{EMM}(t) - \omega_l t + \phi_l\right)}\right]$$

Where $\boldsymbol{u}_0$ is the secular motion amplitude, $\boldsymbol{u}_{EMM}$ is the EMM amplitude, ω_l is the frequency of the laser and ϕ_l is the phase of the laser.

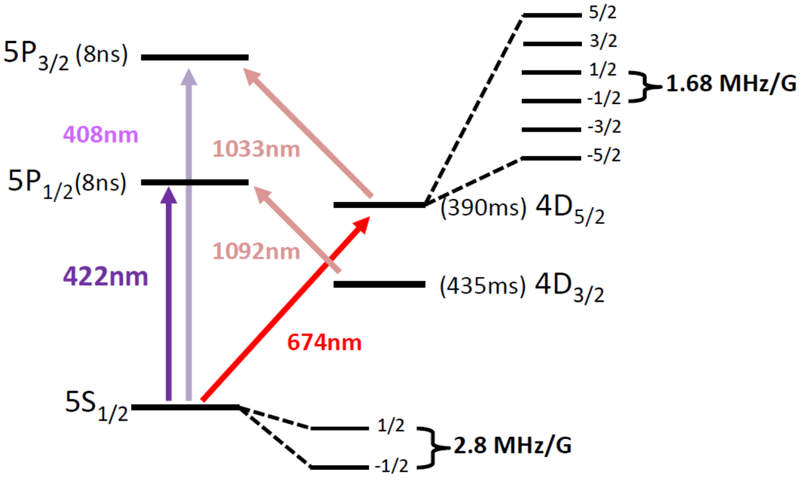

Figure 5: Energy levels scheme of $^{88}Sr^{+}$ ion and the corresponding wavelengths of the transitions. The lifetime of each level is indicated in parenthesis. 422nm and 1092nm dipole transitions are used for Doppler cooling and detection. 674nm quadrupole transition is used to coherent control of the ion: spectroscopy, thermometry and ground-state cooling (with the 1033nm laser).

We can write:

$$\boldsymbol{k}\cdot\boldsymbol{u}_{EMM}\left(t\right)=\beta\cos\left(\Omega t+\delta\right)$$

rewriting the electric field using a Bessel function series expansion $e^{i\beta\cos(\Omega t+\delta)}=\sum_{n}J_{n}\left(\beta\right)e^{in\left(\Omega t+\delta+\frac{\pi}{2}\right)}$:

$$E_{laser}\left(t\right)=\Re\left[E_{0}\sum_{n}J_{n}\left(\beta\right)e^{i\left(\left(n\Omega-\omega_{l}\right)t+n\delta+n\frac{\pi}{2}+\phi_{l}\right)}\right]$$

In the limit $\beta\ll1$ to first order in β: $J_{0}\left(\beta\right)\approx1,J_{\pm1}\left(\beta\right)\approx\frac{\beta}{2}$ and $J_{|n|>1}\left(\beta\right)\approx0$. Since the Rabi frequency is proportional to the electric field, the ratio between the Rabi frequencies of the EMM sideband transitions $(\omega=\omega_{l}\pm\Omega)$ and the carrier transition $(\omega=\omega_{l})$ is given by:

$$\frac{\Omega_{\pm1}}{\Omega_{0}}=\frac{J_{1}\left(\beta\right)}{J_{0}\left(\beta\right)}\approx\frac{\beta}{2}=\frac{\boldsymbol{k}\cdot\boldsymbol{u}_{EMM}}{2}$$

Hence, by measuring the coupling of the EMM sideband and the carrier, we can find the projection of the amplitude of the EMM on the beam direction. In order to measure the EMM and minimize it on the radial plane, two 674nm beams were used, which have orthogonal projections on the radial plane.

As described before, the in-phase EMM in the radial plane is due to stray electric field, Therefore, in order to minimize it, there are two perpendicular dc compensation electrodes that enable to move the ion in the direction of the two beams projections. By finding the shelving probability for different compensation voltages, we can find the lowest coupling to the EMM sideband and hence minimize the EMM. See Fig. (6) for an example. However, when scanning the compensation voltage for transitions between different Zeeman sublevels, the optimal compensating voltage is changed. This is because the Zeeman shift of each level also oscillates the the rf frequency and contribute to the sideband at $\omega_l \pm \Omega$. However, this shift is opposite for $S_{\frac{1}{2}}\left(m=-\frac{1}{2}\right) \rightarrow D_{\frac{5}{2}}\left(m=-\frac{5}{2}\right)$ and $S_{\frac{1}{2}}\left(m=\frac{1}{2}\right) \rightarrow D_{\frac{5}{2}}\left(m=\frac{5}{2}\right)$ and hence the mean compensation voltage value of these two transition was taken.[9] The same procedure is applied also to the second dc electrode. The minimization of EMM in the axial direction is similar, but with scanning an amplitude and phase of additional rf resonator.

The EMM might drift in time and hence this procedure is preformed every an hour during the experiment in order to maintain it sufficiently low. An analysis of the EMM before and during the experiment is described in appendix A.

3.2.2 Ion initialization and detection

Doppler cooling When the ion is trapped it is initially very hot. In order to cool it down, we use Doppler cooling on the strongly allowed transition${}^5S_{\frac{1}{2}} \rightarrow {}^5P_{\frac{1}{2}}$ at 422nm. Since the ion can decay from ${}^5P_{\frac{1}{2}}$ level to long lived ${}^4D_{\frac{3}{2}}$ level, a repump laser at wavelength of 1092nm is applied during Doppler cooling. On the first stage of the cooling, 1 ms far-off-resonce (240MHz red detuned) pulse is applied and then additional near-resonance 1 ms pulse is applied. The near-resonance frequency depends on the specific spectrum of the transition which depends also on the repump laser parameters. The limit of the Doppler cooling is given by the recoil limit:

$$T_{Doppler} = \frac{\hbar\Gamma}{4k_B}$$

For the ${}^5S_{\frac{1}{2}} \rightarrow {}^5P_{\frac{1}{2}}$ transition $\Gamma = \frac{1}{2\pi}\frac{1}{8ns}$ in the linewidth of the ${}^5P_{\frac{1}{2}}$ level. hence $T_{Doppler} \approx 40\mu K$

---

[9] The shift is proportional to $\Delta\nu \propto -g_J\left({}^2S_{\frac{1}{2}}\right)m_S + g_J\left({}^2D_{\frac{5}{2}}\right)m_D$ with g_J are the Landé g-factor for each level and $m_S\,(m_D)$ is the component of the total angular momentum in the direction of the magnetic field of the $S_{\frac{1}{2}}\left(D_{\frac{5}{2}}\right)$ level.

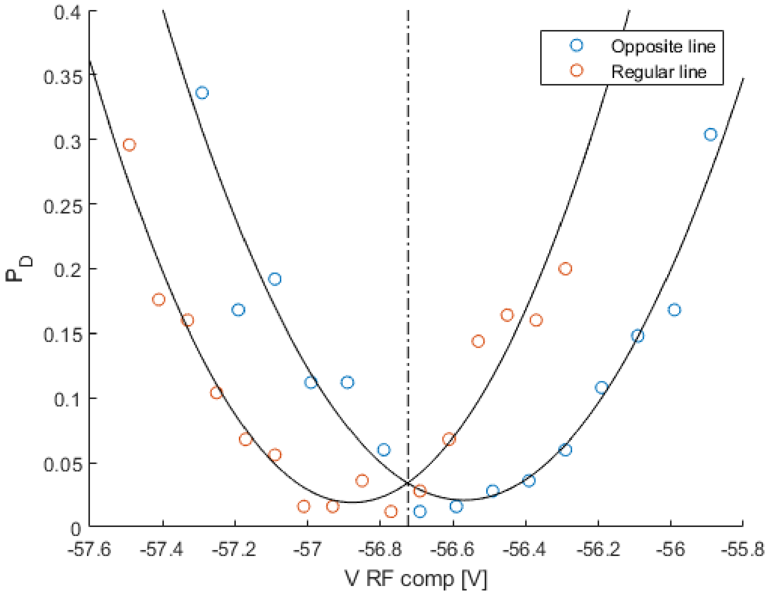

Figure 6: Example of an EMM minimization. Shelving probability for two rf frequency sideband transitions with opposite Zeeman shifts as function of the voltage on one of the compensation electrodes. The transition are: $S_{\frac{1}{2}}\left(m=-\frac{1}{2}\right) \to D_{\frac{5}{2}}\left(m=-\frac{5}{2}\right)$ (red) and $S_{\frac{1}{2}}\left(m=\frac{1}{2}\right) \to D_{\frac{5}{2}}\left(m=\frac{5}{2}\right)$ (blue). When the EMM is compensated, the coupling to the rf sideband is minimal, which corresponds to minimal shelving probability. However, this occurs at different compensation values for different transitions due to oscillating Zeeman shift induced by the rf field (see text). The mean value of voltage for different opposite transitions is taken as the real compensation value (vertical line).

for $\omega \sim 1MHz$ motional frequency we get $\bar{n} \sim 1$.

Ground state cooling In order to get rid of the remaining motional quanta and get into the ground motional state, resolved-sideband cooling was used. In this method, the motional sidebands were initially found. Then 3 pulses were applied sequentially for each of the 3 motional modes:

1. 674nm on the red sideband of the $5S_{\frac{1}{2},-\frac{1}{2}} \rightarrow 4D_{\frac{5}{2},-\frac{5}{2}}$ transition - this reduces a single motional quanta.

2. 674nm on the $5S_{\frac{1}{2},\frac{1}{2}} \rightarrow 4D_{\frac{5}{2},-\frac{3}{2}}$ optical pumping transition - in order to re-pump the population to $5S_{\frac{1}{2},-\frac{1}{2}}$ level.

3. 1033nm repump to $4D_{\frac{5}{2}} \rightarrow 5P_{\frac{3}{2}}$ transition - from the $5P_{\frac{3}{2}}$ level the ion decays to $5S_{\frac{1}{2}}$.

this pulse scheme was applied a few times until most of motional modes were removed and the average phonon occupation was $\bar{n} < 0.1$ in all motional modes.

Detection After applying a 674nm shelving pulse, the ion will be in some superposition of the $5S_{\frac{1}{2}}$ and $4D_{\frac{5}{2}}$ states. In order to measure it, the 422nm and 1092nm lasers are turn on for 1ms. If the state collapses to the $5S_{\frac{1}{2}}$ state, the ion will scatter photons and will appear “bright”. Otherwise, it collapses into the $4D_{\frac{5}{2}}$state which is a “dark” state. Repeating this detection scheme enables us to find the probability to be in the ground $5S_{\frac{1}{2}}$ state or the excited $4D_{\frac{5}{2}}$ state.

Trap frequencies measurements The trap frequencies are necessary in order to ground-state cool the ion and find its temperature. These frequencies are different for each configuration of the trap parameters. They were measured in two different methods:

1. Scanning the relevant sideband transition with the 674nm laser.

2. Inducing oscillating electric field with varying frequency. Driving the ion in its resonance motional frequencies will enhance its energy and hence will cause a reduction in its fluorescence (due to larger Doppler shift).

These two methods will give a slightly different values, since measuring with the 674nm introduces a light shift. However, this shift also needs to be accounted for when applying ground-state-cooling pulses. Examples for measurements are shown in Fig. 7.

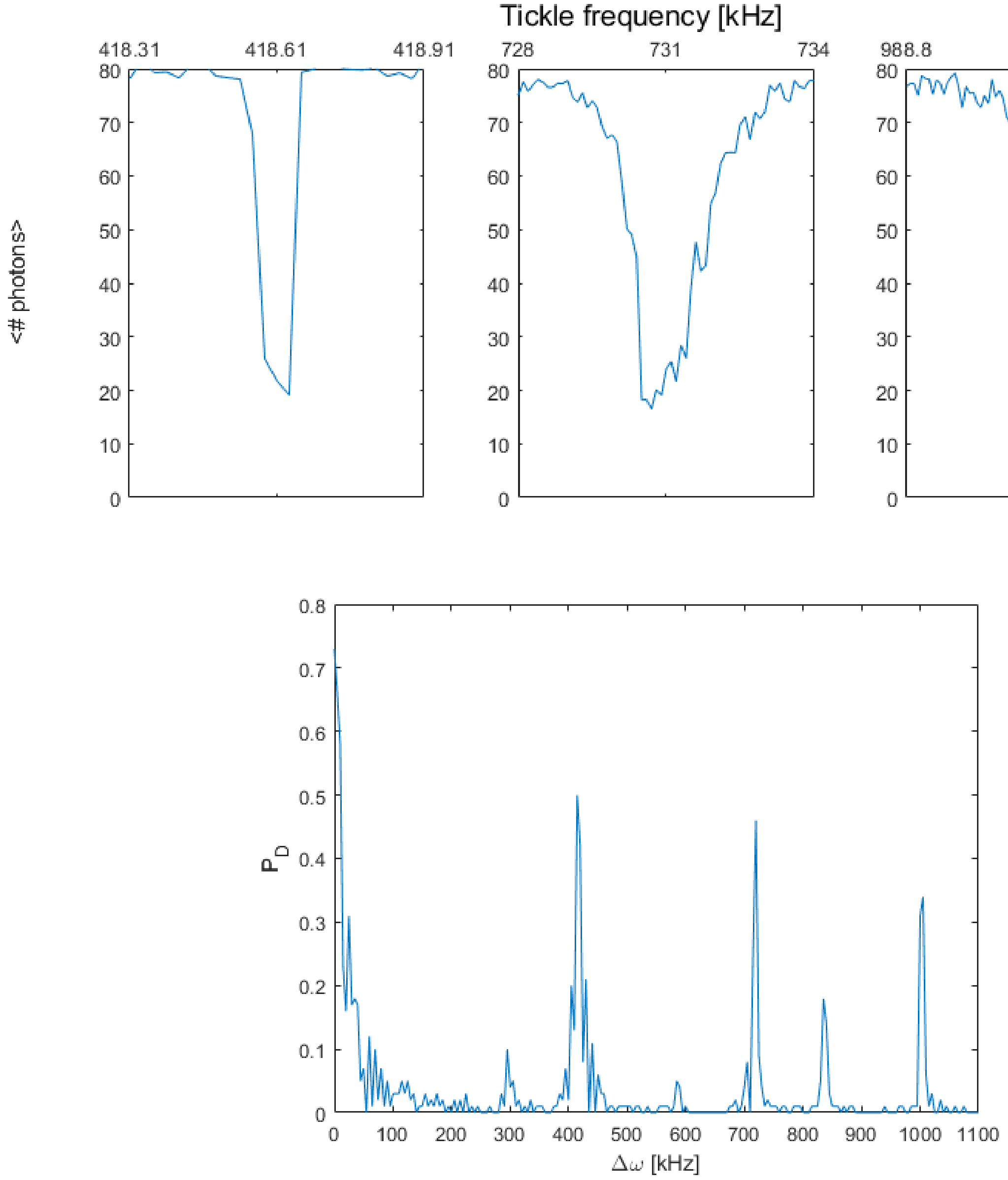

Figure 7: Examples of a trap frequencies measurements ($418kHz$ axial and $731, 990kHz$ radials) . (a) The fluorescence of the ion when scanning the frequency of a driven electric field. The fluorescence decreases when the frequency is in resonance with a frequency of the secular motion. (b) Shelving probability as function of detuning of the laser from the carrier frequency. The secular motion modulates the laser frequency and gives rise to sidebands at the secular motion frequencies. higher orders of this coupling is also visible (e.g. twice the axial frequency at $\approx 840kHz$). In this method the frequencies are shifted due to light shift.

3.2.3 Thermometry

There are several methods for finding the occupation of the different quantum oscillator levels for all modes. In the regime of few μK to few mK carrier Rabi Thermometry can be used.

When exciting a carrier transition ($\delta = 0$) with the 674nm laser, the shelving probability of the excited state ("dark state") for the n-th level is given by[10]:

$$P_D\left(t_R;\boldsymbol{n}\right) = \sin^2\left(\Omega_{\boldsymbol{n},\boldsymbol{n}} t_R\right)$$

Where $\boldsymbol{n}$ is the harmonic oscillator level (in each of the 3 modes), t_R is the time of the 674nm pulse and the coupling strength $\Omega_{\boldsymbol{n},\boldsymbol{n}}$ is defined as:

$$\begin{aligned} \Omega_{\boldsymbol{n},\boldsymbol{n}} &\equiv \Omega_0 \left| \langle n| \exp\left\{ i\sum_j \eta_j \left(\hat{a}_j e^{-i\nu t} + \hat{a}_j^\dagger e^{i\nu t}\right)\right\} |n\rangle \right| \\ &= \Omega_0 \Pi_j e^{-\frac{\eta_j^2}{2}} L_{n_j}\left(\eta_j^2\right) \end{aligned} \tag{14}$$

Where $L_n\left(x\right)$ is Laguerre polynomial of order n, Ω_0 is the rabi frequency at the ground state and η_j are the Lamb-Dicke parameters for each mode. The two last values are measured in the experiment.

However, the ion has an energy distribution and hence the population is divided over many harmonic oscillator levels. Then the probability to be in the excited state is:

$$P_D\left(t_R\right) = \sum_{\boldsymbol{n}} P\left(\boldsymbol{n}\right) \sin^2\left(\Omega_{\boldsymbol{n},\boldsymbol{n}} t_R\right) \tag{15}$$

Where $P\left(\boldsymbol{n}\right)$ is the energy distribution.

However, in our case the probability is given as a function of the total energy $P\left(E\right)$. In the classical limit when $\bar{n} \gg 1$ we can use the relation:

$$E_i\left(n_i\right) = \hbar\omega_i\left(n_i + \frac{1}{2}\right) \approx \hbar\omega_i n_i \tag{16}$$

---

[10] The ion is initialized at its ground electronic state

where E_i is the energy in the i-th mode.

The summation over the n's is preformed by taking logarithmic spaced n's for each mode up to some cutoff value, then the corresponding Rabi frequency is calculated by Eq. (14) and the corresponding total energy by Eq. (16). The probability for this term is taken from the predefined $P\left(E\right)$ probability (Thermal, Tsallis or numerical).

In order to reduce the integration time, the 3D sum in Eq. (15) can be calculated as a 1D integral:

$$P_D\left(t_R\right) = \int_E P\left(E\right)\sin^2\left(\Omega\left(E\right)t_R\right)$$

This calculation is preformed for any pulse time t_R.

As a rule of thumb, "cold" ion will give a high contrast sine-square function, whereas "hotter" ion shows dephasing which is faster as the temperature is higher. See Fig. 8 for examples of theoretical calculation of Rabi flops of different temperatures (assuming underlying thermal distribution).

This method can be used for finding temperatures ranging between few μK to few mK. However, the sensitivity on the boundaries is low since it is limited by the signal-to-noise ratio of the measurement.

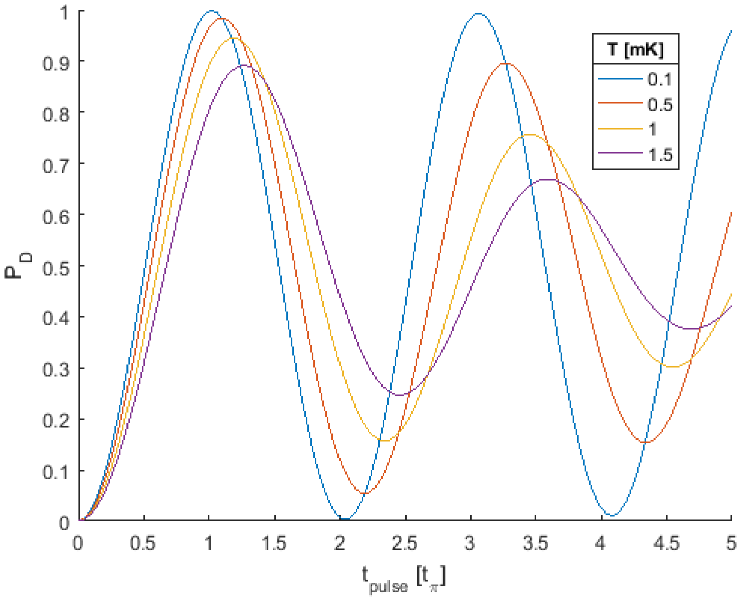

Figure 8: Carrier Rabi Thermometry. Calculated Rabi flops assuming different thermal distributions. Time in units of pi time $t_\pi = \frac{\pi}{2\Omega}$. As larger the energy the de-coherence is larger.

4 Heating dynamics

Cetina et al. [20] derived an expression for the heating of the ion in the first collision. In order to see how the heating mechanism affects the ion energy beyond the first collision, the simulation that includes the polarization potential was run with many consecutive collisions. Preforming many realizations up to some predefined time enables to calculate numerically the energy distribution of the ion. Results for such a simulation are shown in Fig. (9). As can be seen, the energy distribution is changing its behavior during the interaction with the atoms. Not only that the most likely energy is increasing, but also the high-energies part of the distribution is developed into a power-law. In addition, the energy distribution doesn't change after ~30ms means that the system is entering a steady state.

The steady state distribution cannot be described exactly as thermal distribution nor Tsallis distribution . However, Tsallis distribution can provide a reasonable approximation by only 2 free parameters. These parameters are time-dependent as can be seen in Fig. 10. In order to quantify these two parameters in a single number $T_{ion} = T\frac{n}{n-2}$. It can be seen that the power law becomes stable after few collisions, whereas the ion continues to heat up.

The system is heating from the initial conditions to a steady state in a 1/e time of 7.26 ms, which corresponds to ~16 collisions on average.

As described before, the major contribution to the heating is due to hard-sphere collisions, and not glancing collisions. As can be seen in Fig. 11(a), in the first collision the histogram is highly asymmetric around zero. This indicates that there is much more gain than loss, which leads to heating. This effect is less prominent for the subsequent collisions but the gain or loss can be much larger, even an order of magnitude larger than the initial energy of the ion or the atoms temperature. This can be explained by the fact that in the first collision, the polarization potential moves the ion considerably from the center of the trap whereas in the subsequent collisions this effect is smaller. The amount of energy the ion can gain (or lose) depends on the energy the ion had before the hard-sphere collision (Fig. 11(b)). Also here there is an asymmetry between the gain and loss: the ion cannot lose more energy than its initial energy, but it can gain much more. As before, at the low energies, this effect is more dominant.

4.1 Trap parameters dependence

The heating dynamics in presence of EMM depends on which trap parameters are used. Also when the heating comes from the effect of the attraction from the polarization potential it changes the heating,

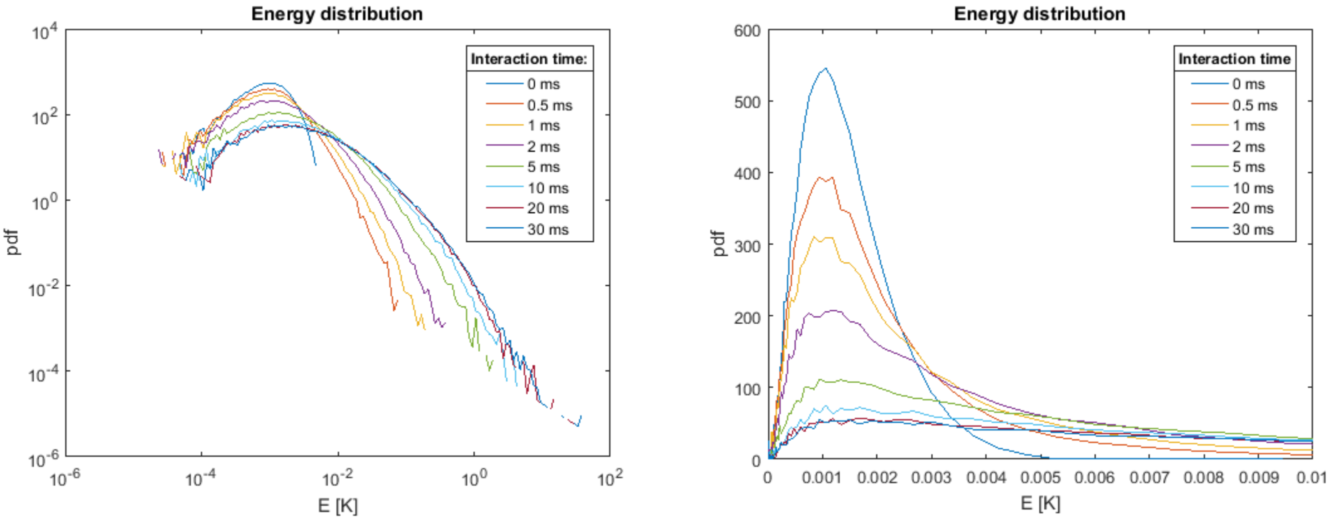

Figure 9: Heating due to polarization potential. This simulation was run with 50,000 repetitions up to 100ms interaction time for atom density of $1.2 \cdot 10^{12} cm^{-3}$ at temperature of $6 \mu K$. The ion was initialized with energy of $0.5 mK$ (equally divided in all 3 motional modes). EMM was not taken into account in this simulation. At 30ms the system has already entered the steady state. Both histograms was taken in logarithmic bins. Normalization is taken with respect of the total number of repetitions. (left) log scale. (right) linear scale.

see Eq. (11). In order to see how the polarization potential affects beyond the first collision, we run the simulation with different trap parameters. The trapping can be described generally by two parameters, q - which describes the radial rf confinement and a - which describes the axial dc confinement. Assuming a perfect symmetric Paul trap (without bias voltage), we can see how these parameters effect the heating dynamics in Fig. 12.

The rf confinement induces larger heating rates on both high and low voltages as can be seen in Fig. 13(b). The rf parameter also gives the same trend in the temperature parameter ($T_{Tsallis}$) in steady state (Fig. 13(d)). This can be explained by the fact that high rf confinement leads to larger electric fields that can do more work during a collision and hence can cause more heating. On the other hand, when q is low, the trap is shallow in the radials directions and then the collision occurs in higher electric fields. As a consequence, there is a a point where the heating is minimal. This larger energy scale is also maintained in steady state.

For the dc confinement, the heating rate is larger for tighter axial confinement, with similar trend of

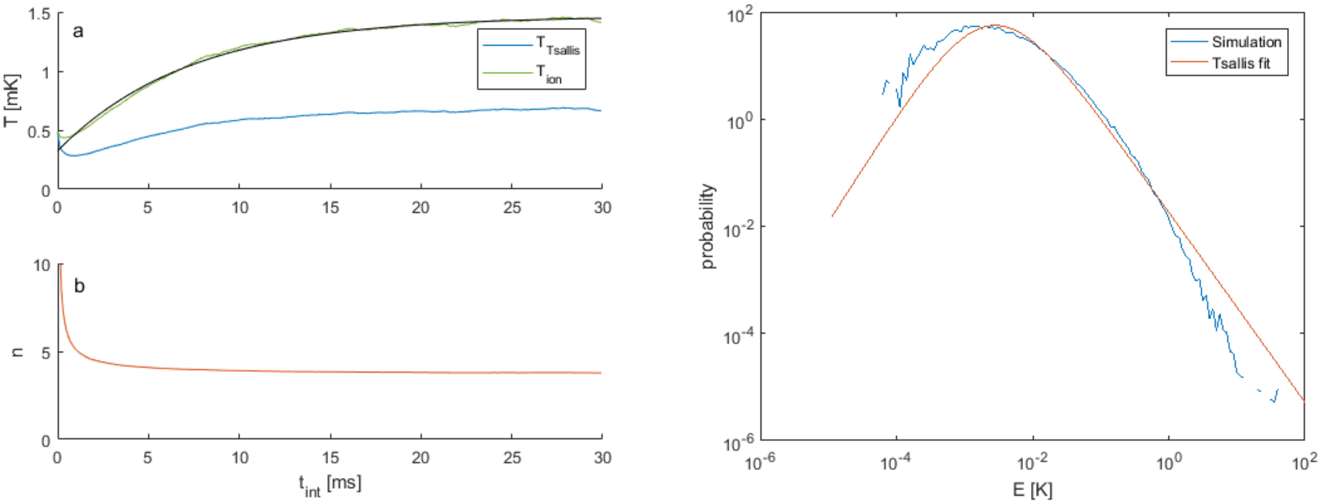

Figure 10: Heating and power-law development. (left) Time evolution of Tsallis free parameters n (a) and T (b) and ion's temperature T_{ion} (b). For each time step the energy distribution was fitted to Tsallis distribution using maximal likelihood estimation. From exponential fit, the heating rate is $157\frac{\mu K}{ms}$ which is equivalent to $96.78\frac{\mu K}{coll}$ with a numerical Langevin rate of $2.25\frac{coll}{ms}$. The steady-state energy is $T_{ion}^{steady-state} = 1.45mK$. (right) Steady-state distribution for molecular dynamics simulation with a fit to Tsallis distribution (using MLE) with $T = 663(4)\mu K$ and $n = 3.775(3)$. Fitting to a thermal distribution gives $23\,(1)\,mK$ (not shown).

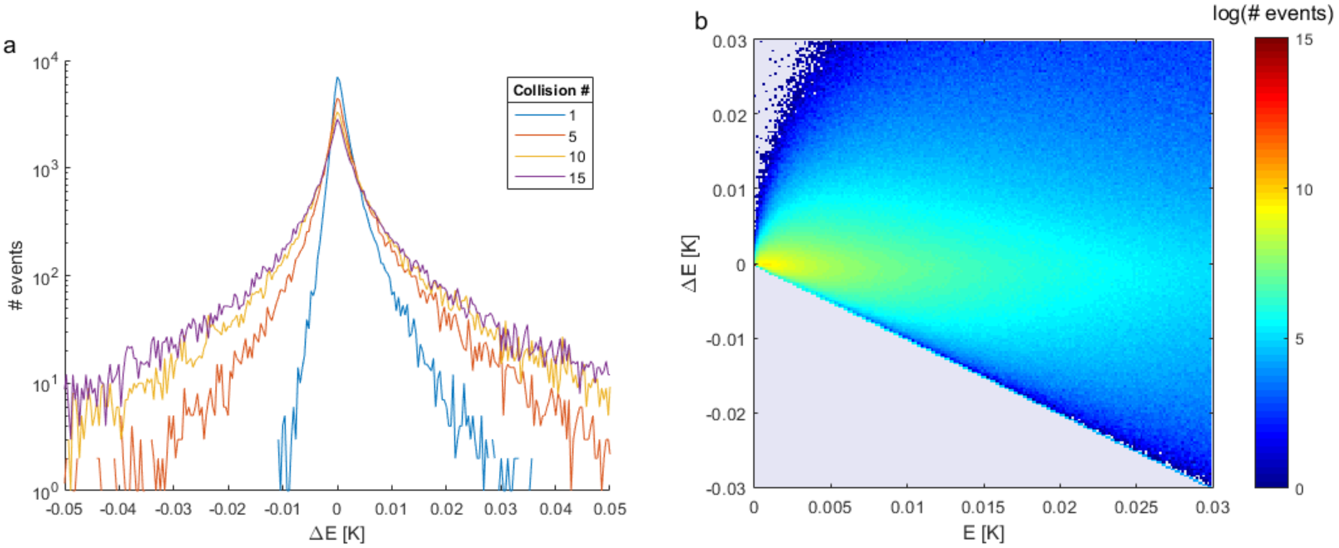

Figure 11: Energy gain in a hard-sphere collision. The simulation was run with the experimental parameters described in Ref. [21]. The total number of realizations is 50,000. Only hard-sphere collisions (minimum ion-atom distance of less than 5nm occurred at least one time) were taken into account. (a) Histogram of energy gain or loss ΔE after a constant number of collisions. (b) Histogram of energy gain or loss ΔE as function of the energy before the collision. Number of events is given in a log scale. All the hard-sphere collisions events were taken into account.

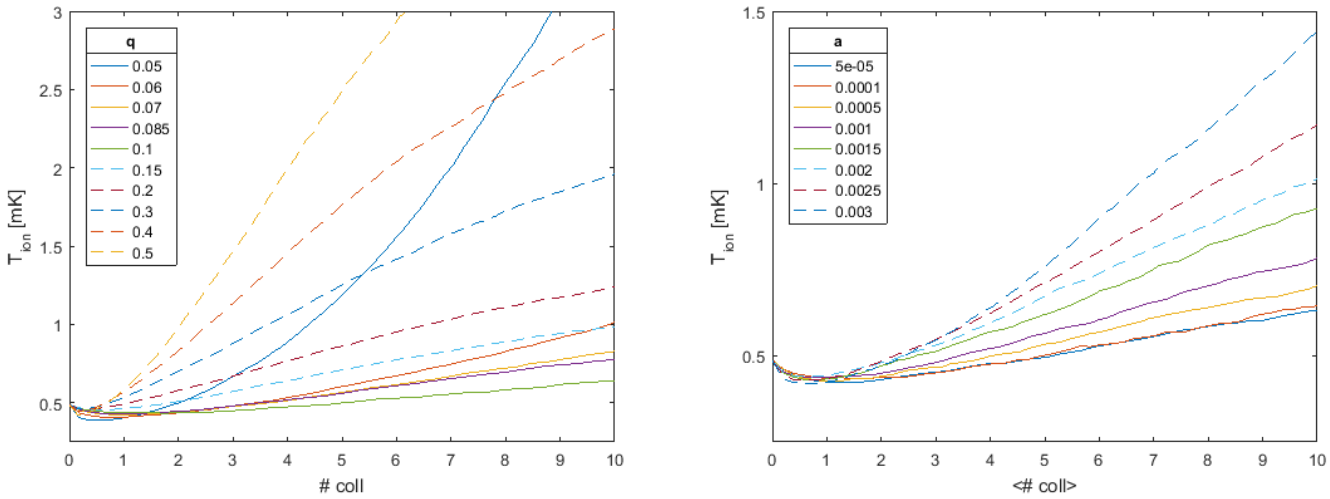

Figure 12: Ion's energy as a function of time (counted in hard-sphere collisions) when trap parameters are changed. (left) changing the rf confinement ($q \propto V_{RF}$) with a constant axial confinement $a = 0.001$ (right) changing the dc confinement ($a \propto V_{DC}$) with a constant rf confinement $q = 0.1$. In these simulations the trap was a perfect linear Paul trap, i.e. $\vec{a} = (-a, -a, 2a)$ and $\vec{q} = (-q, q, 0)$.

the steady state temperatures (Fig. 13(a,c)). This can be explained by the fact that axial confinement induces static radial de-confinement, which is equivalent to decreasing the dynamic radial confinement without reducing the rf field. As before, more shallow radial confinement enables the collision to occur at larger distances and hence the rf field can preform more work.

Loose radial confinement (whereas it come from dc or rf) will lead to a more dominant power-law tail at steady-state (Fig. 13(e,f)).

4.2 Experimental results

The heating rates for different trap parameters were also measured experimentally. One major challenge in these measurements arises due to the fact that in order to find the energy distribution after a specific interaction time, a couple of hours of integration time were needed. Hence, for each set of trap parameters, three interaction times were chosen. The first one is immediately after the ground-state cooling without interaction with atoms. The other two, were with different times of interaction with the atoms. These two points were chosen such that the ion will not get into the steady state regime, where the

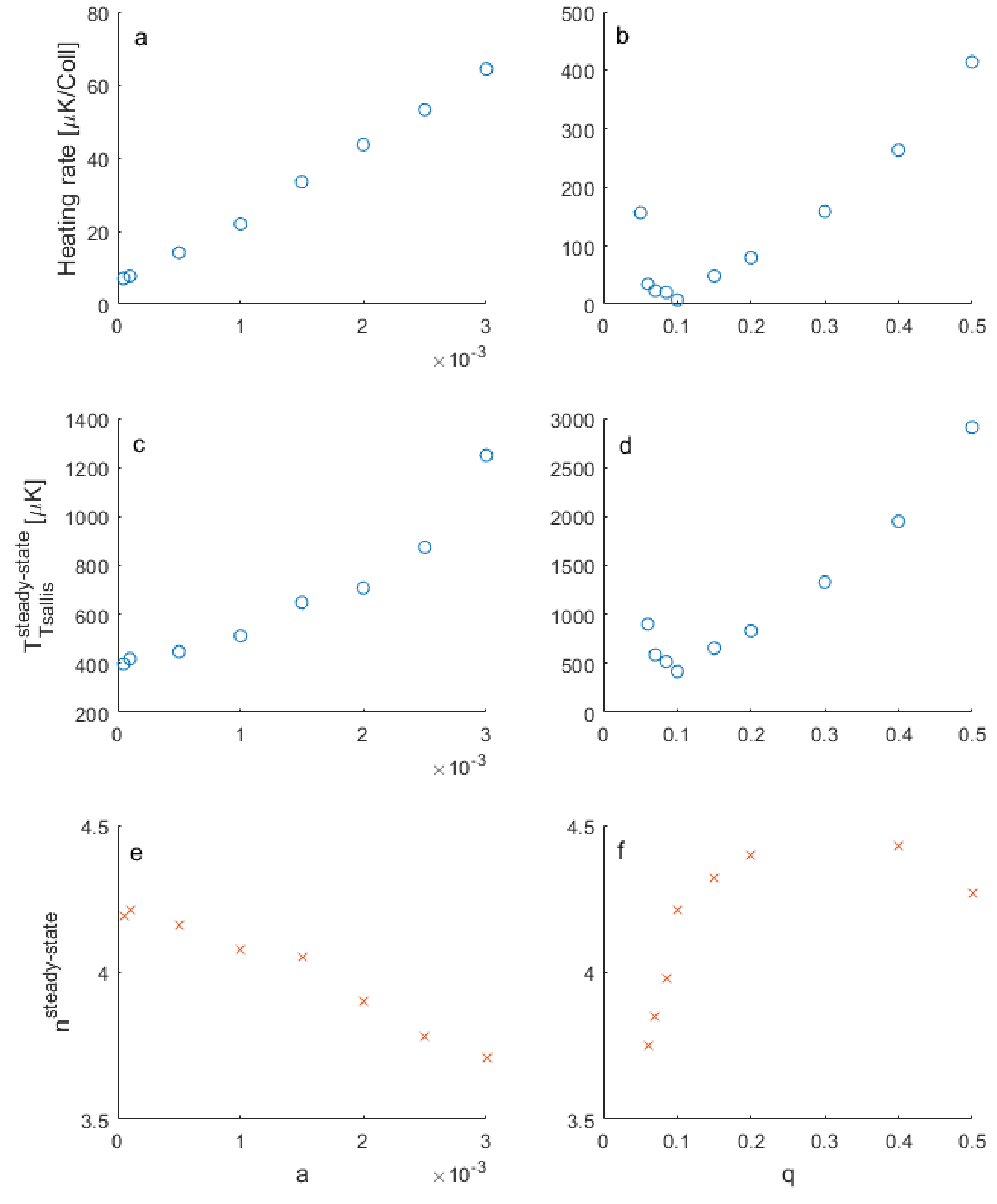

Figure 13: Heating rates and parameters of steady state energy distribution for different trap parameters. (a,c,e) different rf confinements with constant dc ($a = 0.001$). (b,d,f) different dc confinements with constant rf ($q = 0.1$). (a-b) Mean ΔT_{ion} per collision calculated for the first five hard-sphere collisions. (c-d) Tsallis temperature at steady state. (e-f) power-law parameter of the Tsallis distribution at steady state. All values were calculated by preforming MLE to Tsallis distribution.

resolution of the thermometery is lower. Moreover, the Rabi pulse times were chosen to be the points which exhibit the largest change when the temperature is changed. This enabled us to minimize the number of points which was taken at each Rabi flop to five and hence reduce the experiment time.

For each interaction time, Rabi flop was taken with approximately 90 repetitions for each pulse time. In order to simplify the fitting process, each interaction time was fitted with a single fitting parameter. For the first point, thermal distribution was assumed. For the two other point, Tsallis distribution with $n = 4$ was assumed. As seen in the previous section, the power law n of the distribution converged quickly into a constant value closed to $n = 4$, and hence taking this as a constant will not change significantly the result. The fit was preformed using maximal likelihood estimation (MLE). The likelihood function is defined as:

$$L\left(P\left(E\right)\mid\left\{x_i,N_i\right\}\right)=\Pi_i\binom{N_i}{x_i}p_i^{x_i}\left(1-p_i\right)^{N_i-x_i} \tag{17}$$

Where i is the index of the Rabi pulse time, N_i is the number of repetition for the i-th pulse time, x_i is the number of dark events and p_i is the probability to get dark state at the i-th pulse time. The p_i's depend on the underlying distribution $P\left(E\right)$ and are calculated using Eq. (15). Taking the log-likelkihood:

$$\log L\left(P\left(E\right)\mid\left\{x_i,N_i\right\}\right)=\sum_i\log\binom{N_i}{x_i}+\sum_i\left[x_i\log p_i+\left(N_i-x_i\right)\log\left(1-p_i\right)\right]$$

Note that the first term is independent of the underlying distribution and hence does not have to be considered in the maximization process. Error bars of 1σ were calculated from the $\log L$ function. An example of such a fitting process is displayed in Fig. 14.

In contrast to the results presented in Figs. 12 and 13 that was taken assuming a perfectly symmetric Paul trap, in the experiment the radial frequencies cannot be degenerate due to cooling limitations. Hence, a bias voltage was applied in order to get frequency difference of about $\sim 100\,\mathrm{kHz}$ between the radial modes. This bias voltage weakly depends on the chosen trap parameters.

For each set of trap parameters, the EMM was compensated before and during the experiment (about every hour). An upper bound to the EMM energy that remains in the system after a compensation can be calculated from the minimization process (see appendix Afor details). In addition, between two minimization processes, the compensated values of the voltages drift. This also enters EMM that

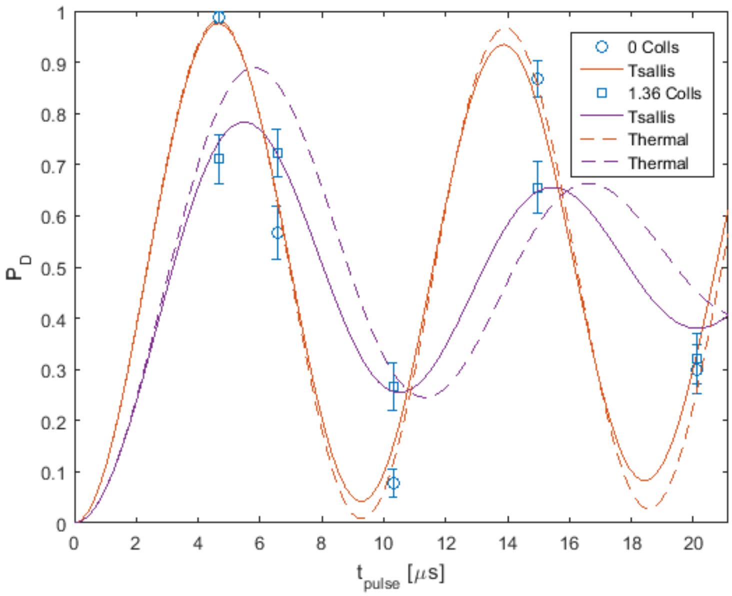

Figure 14: Fitting to thermal and Tsallis distribution. 2 Rabi flop at different interaction time ($t_1 = 0\,\mathrm{ms}$ and $t_2 = 4\mathrm{ms} = 1.36Colls$) taken for trap parameters of $V_{DC} = \mathrm{V}250V$ and $V_{RF} = 505\mathrm{V}$. The fitting was performed using MLE process as described in the text. There error bars for the experimental data are standard deviation of binomial distribution $\sigma = \sqrt{\frac{p(1-p)}{n}}$. The same analysis was preformed to all measurements in different trap parameters.

depends on the change of the voltages. Summary of the EMM values is shown in table 1. It seems that the EMM which enters from drifting is much smaller than the remaining EMM after compensation.

The temperatures for different interaction times in different trap parameters are shown in Fig. 15(a). At each interaction time, a Tsallis temperature was extracted from the Rabi flop data by MLE as described before. An estimated heating rate of each experiment was calculated by fitting a linear line. All experiments give roughly the same heating rates in the order of 100-200μK . Comparing to the numerical simulation results with the same experimental parameters reveals that a couple of differences. First, the heating in the experiment is much more faster than the prediction of the simulation. The estimation of the mean number of collisions in the experiment is by measuring the atomic density using TOF analysis. This can enter a factor of order two in the density, for example by error in estimating the magnification of the camera. However, this is a constant factor for all densities and hence, only scales the abscissa. Second, the simulation predicts only a minor difference in temperature between different experiments (less than $50\mu K$), with a slightly higher heating rate for the higher rf confinement. However, in the experiment, the heating in shallow rf confinement is higher than most of the other experiments.

The numerical simulation did not take into account the remaining EMM after compensation, which is different between the experiments (see Table 1). Preforming a simulation of the two extreme rf confinements (rf 16 and 21) with EMM equivalent to $50\mu K$ reveals that even this small amount of uncompensated energy can cause a larger shift the temperatures than the shift that is caused by changing the trap parameters, see Fig. 16. However, this is still much smaller than the estimated EMM after compensation. Simulation with residual EMM of $\sim 1mK$ predicts heating rates that are larger in order of magnitude (not shown), which indicated that the residual EMM energy after compensation are overestimated.[11] Hence, the deviations between the experiments, and compared to the simulation can be attributed to uncompensated EMM of few tens of μK, which is the order of magnitude of controlling EMM compensation in the system.[12]

---

[11] These values are very sensitive to calibration of the carrier transition π time, which was taken in this estimation from a flop of a Doppler-cooled ion. The difference in the π time of a Doppler-cooled ion and a ground state cooled ion can be significant.

[12] See residual EMM budget in Ref. [25].

	$T_{EMM}\ [\mu K]$	$T_{EMM}^{RF}\ [\mu K]$	$T_{EMM}^{GND}\ [\mu K]$
RF 18 (1st exp.)	1123	5	81
RF 18 (2nd exp.)	1014	274	39
RF 16	1971	70	9
RF 21	430	3	0.5
DC 390V	690	339	76
DC 600V	1250	43	186

Table 1: EMM temperature in each experiment. T_{EMM} is the estimated temperature at the beginning of each experiment. T_{EMM}^{RF} (T_{EMM}^{GND}) is the EMM that energy from drifting of the static electric field in the direction of RF (GND) electrode. See Appendix A for more details.

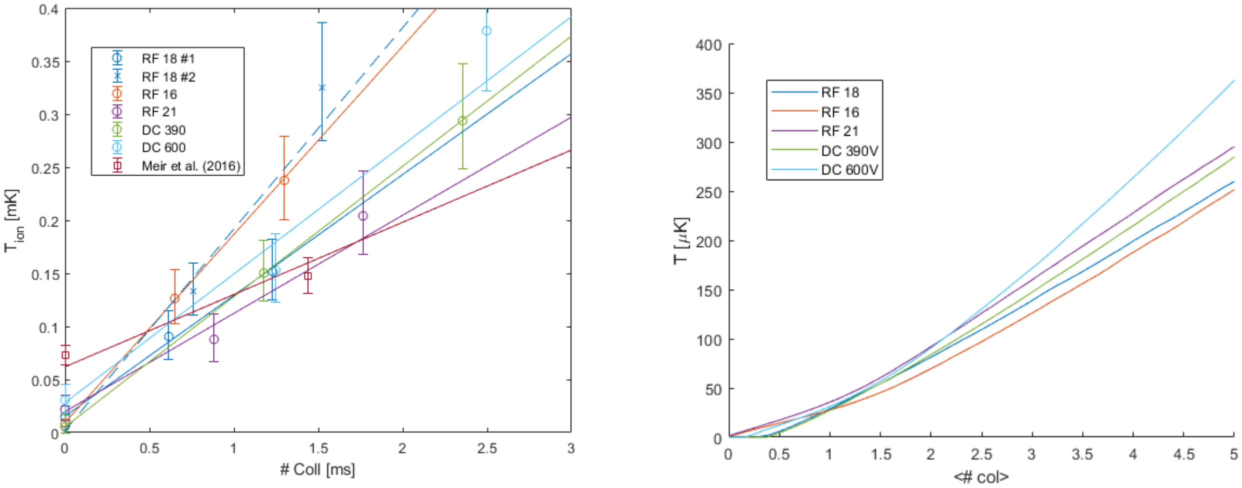

Figure 15: Heating rates for different trap parameters. (left) Temperatures for different mean number of collisions for different trap parameters as measured in experiment. Each temperature was extracted from the Rabi flop data by fitting to a Tsallis distribution with $n = 4$. Error bars are 1σ calculated from the likelihood function. Solid lines are linear fits for each experiment, with heating rates given in Table 2. (right) The heating rates as given by the molecular dynamics simulation. At each time the expected Rabi flop was calculated from the numerical distribution and then fitted to Tsallis (n=4) distribution in the same procedure as in the left graph.

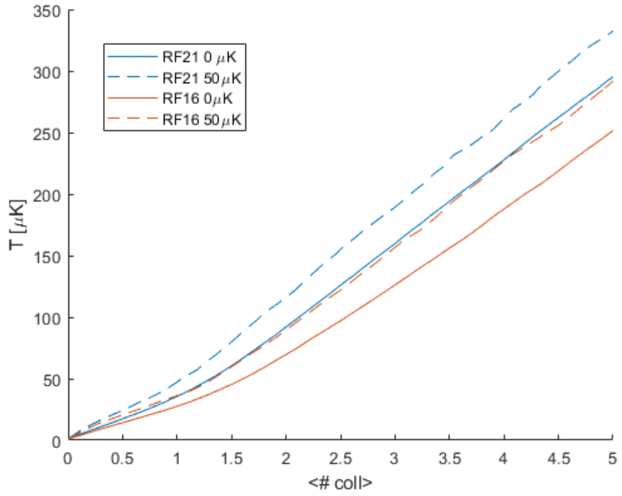

Figure 16: Simulation including EMM in addition to the atom-ion polarization interaction.

	$T_0[\mu K]$	$\Gamma[\frac{\mu K}{Coll}]$
RF 18 (1st exp.)	15(6)	114(12)
RF 18 (2nd exp.)	2(4)	190(36)
RF 16	9(1)	177(4)
RF 21	18(6)	95(18)
DC 390V (comp)	5.3(3)	123(1)
DC 600V	24(32)	119(41)
Meir et al. (2016)	62(27)	68(27)

Table 2: Heating rates and initial temperatures for each experiment extracted by weighted linear fits to the graphs in Fig. 15(a). The error-bars in parenthesis are 1σ. The weights are equal to $\frac{1}{\sigma^2_{T_{ion}(t)}}$.

4.3 Mass ratio heating dependence

The collisional dynamics can be changed for different atom-ion combinations. Choosing lighter atoms and a heavy ion will reduce the effect of pulling the ion from the rf null during the collision. This effect can be easily investigated numerically. The numerical simulation was performed to the following atom-ion systems: $^{174}Yb^+ - {}^7Li$, $^{40}Ca^+ - {}^7Li$, $^{174}Yb^+ - {}^{87}Rb$, $^{138}Ba^+ - {}^{87}Rb$, $^{88}Sr^+ - {}^{87}Rb$. All other parameters, dc and rf confinement and rf frequency, were kept constant. We can see in Fig. 17 that

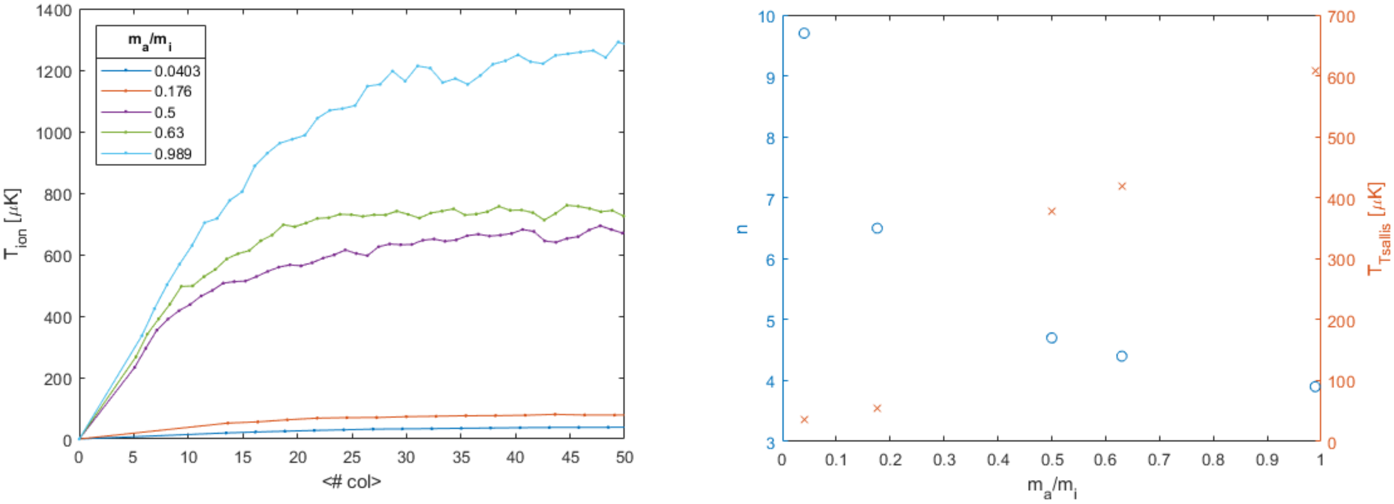

Figure 17: Simulation of the ion heating in different atom-ion systems. The simulation was run with the same trap parameters (a, q and Ω) but with a different atom-ion mass ratio. The combinations are (from low to high atom-ion mass ratio): $^{174}Yb^{+} - {}^{7}Li$, $^{40}Ca^{+} - {}^{7}Li$, $^{174}Yb^{+} - {}^{87}Rb$, $^{138}Ba^{+} - {}^{87}Rb$, $^{88}Sr^{+} - {}^{87}Rb$. The initial ion temperature is $1\mu K$. The numerical energy distribution was fitted to Tsallis distribution using MLE.

choosing a lower atom-ion mass ratio improves the energy distribution by two means: the characteristic temperature is lower, and the power-law tail is less significant. The lower temperature in the systems with ^{7}Li atoms is also due to the reduced polarization of the ^{7}Li relative to the ^{87}Rb.[13] The difference in the polarizability also increase the s-wave limit. As can be seen in Table 3, for systems with ^{87}Rb atoms the s-wave limit is about four or five orders of magnitudes lower than the steady state temperature. In systems with ^{7}Li the s-wave limit is much higher, but still higher than the steady state temperature.

	$\frac{m_a}{m_i}$	$T_{ion}\ [\mu K]$	$E_s\ [\mu K]$
$^{174}Yb^{+} - {}^{7}Li$	0.0403	38	6.400
$^{40}Ca^{+} - {}^{7}Li$	0.176	78	8.178
$^{174}Yb^{+} - {}^{87}Rb$	0.5	680	0.0443
$^{138}Ba^{+} - {}^{87}Rb$	0.63	740	0.052
$^{88}Sr^{+} - {}^{87}Rb$	0.989	1200	0.0778

Table 3: Comparison of steady state temperatures and s-wave limit for different atom-ion systems.

---

[13] $C_4^{Rb} = 10.907 \cdot 10^{-57} J \cdot m^4 C_4^{Li} = 5.6057 \cdot 10^{-57} J \cdot m^4$

5 Discussion

Interactions between ultra-cold atoms with cold ions, in the presence of non rf fields considerably heat up the ion. Minimizing stray electric fields that shift the ion from its null position can reduce this heating but cannot cancel it completely. When the ion is in its null rf position, the inherent physics of the atom-ion attraction causes collisions to occur at non-vanishing rf fields. It was shown theoretically that this effect enters energy in the first collision which depends on the chosen trap configuration: static and dynamic electric fields confinement and atom-ion mass ratio.[20] However, this was restricted to the first collision and did not consider the effect of many collisions, that also showed a non-thermal behavior.[21]

In this work, this effect was investigated numerically and experimentally for different trapping parameters and many collisions. The system is entering steady state with non-thermal energy distribution and the power-law behavior is revealed after a few collisions. Numerically, the system exhibits more significant heating when the rf confinement is too high or too low and when the axial confinement is high. Apparently, in all cases, heating occurs for the same reason - higher non-vanishing rf fields, whether they come from lower radial confinement (low rf or high dc) that cause the collision to occur further from the rf null position, or directly from stronger rf field. In the experimentally available parameters, the numerical simulation predicts that the axial confinement will present negligible effect on the heating and smaller rf confinement will give slightly lower heating. Experimentally, the difference between experiments is not as predicted by the simulation, but can be explained by small residual EMM which is different between experiments.

Numerical analysis of systems with different atom-ion species reveal that, for an heavy ion and light atom (with lower polarizability) the dynamics gives in steady state much lower temperature and less dominant power-law tail. However, the characteristic temperature is still higher than the s-wave limit.

Whereas the heating comes from polarization potential effect or from uncompensated EMM, the Paul trap is limiting the investigation of low energy collisions to interaction times of a few collisions. Different types of ion trapping might diminish this effect. One possible solution can be optical trapping of the ion that was recently implemented for only a limited trapping time.[28]

References

[1] J. I. Cirac and P. Zoller. Quantum computations with cold trapped ions. *Physical Review Letters*, 74(20):4091–4094, 1995.

[2] R. Shaniv, N. Akerman, and R. Ozeri. Atomic quadrupole moment measurement using dynamic decoupling. *Physical Review Letters*, 116(14):1–5, 2016.

[3] E. A. Cornell and C. E. Wieman. Nobel lecture: Bose-Einstein condensation in a dilute gas, the first 70 years and some recent experiments. *Reviews of Modern Physics*, 74(3):875–893, 2002.

[4] Immanuel Bloch, Jean Dalibard, and Wilhelm Zwerger. Many-body physics with ultracold gases. *Reviews of Modern Physics*, 80(3):885–964, 2008.

[5] Michał Tomza, Christiane P. Koch, and Robert Moszynski. Cold interactions between an Yb+ ion and a Li atom: Prospects for sympathetic cooling, radiative association, and Feshbach resonances. *Physical Review A - Atomic, Molecular, and Optical Physics*, 91(4):1–12, 2015.

[6] Humberto Da Silva, Maurice Raoult, Mireille Aymar, and Olivier Dulieu. Formation of molecular ions by radiative association of cold trapped atoms and ions. *New Journal of Physics*, 17, 2015.

[7] M. Aymar, R. Guerout, and O. Dulieu. Structure of the alkali-metal-atom strontium molecular ions: Towards photoassociation and formation of cold molecular ions. *Journal of Chemical Physics*, 135(6), 2011.

[8] Hauke Doerk, Zbigniew Idziaszek, and Tommaso Calarco. Atom-ion quantum gate. *Physical Review A - Atomic, Molecular, and Optical Physics*, 81(1):1–13, 2010.

[9] U. Bissbort, D. Cocks, A. Negretti, Z. Idziaszek, T. Calarco, F. Schmidt-Kaler, W. Hofstetter, and R. Gerritsma. Emulating solid-state physics with a hybrid system of ultracold ions and atoms. *Physical Review Letters*, 111(8):1–5, 2013.

[10] Wolfgang Paul. Electromagnetic traps for charged and neutral particles. *Rev. Mod. Phys.*, 62:531–540, Jul 1990.

[11] F. G. Major and H. G. Dehmelt. Exchange-Collision Technique for the rf Spectroscopy of Stored Ions. *Physical Review*, 170(1):91–107, jun 1968.

[12] Ralph G. DeVoe. Power-law distributions for a trapped ion interacting with a classical buffer gas. *Physical Review Letters*, 102(6):1–4, 2009.

[13] Constantino Tsallis. Possible generalization of Boltzmann-Gibbs statistics. *Journal of Statistical Physics*, 52(1-2):479–487, 1988.

[14] I. Rouse and S. Willitsch. Superstatistical Energy Distributions of an Ion in an Ultracold Buffer Gas. *Physical Review Letters*, 118(14), 2017.

[15] Kuang Chen, Scott T. Sullivan, and Eric R. Hudson. Neutral gas sympathetic cooling of an ion in a Paul trap. *Physical Review Letters*, 112(14):1–5, 2014.

[16] Michal Krych and Zbigniew Idziaszek. Description of ion motion in a Paul trap immersed in a cold atomic gas. *Physical Review A - Atomic, Molecular, and Optical Physics*, 91(2):1–10, 2015.

[17] Christoph Zipkes, Stefan Palzer, Lothar Ratschbacher, Carlo Sias, and Michael Köhl. Cold heteronuclear atom-ion collisions. *Physical Review Letters*, 105(13):1–4, 2010.

[18] Christoph Zipkes, Lothar Ratschbacher, Carlo Sias, and Michael Kohl. Kinetics of a single trapped ion in an ultracold buffer gas. *New Journal of Physics*, 13, 2011.

[19] D. J. Berkeland, J.D. Miller, Bergquist, Itano, and Wineland. Minimization of ion micromotion in a Paul trap. *J Appl Phys*, 1998.

[20] Marko Cetina, Andrew T. Grier, and Vladan Vuletić. Micromotion-induced limit to atom-ion sympathetic cooling in Paul traps. *Physical Review Letters*, 109(25):1–5, 2012.

[21] Ziv Meir, Tomas Sikorsky, Ruti Ben-Shlomi, Nitzan Akerman, Yehonatan Dallal, and Roee Ozeri. Dynamics of a Ground-State Cooled Ion Colliding with Ultracold Atoms. *Physical Review Letters*, 117(24):1–7, mar 2016.

[22] D. A Steck. Rubidium 87 d line data. *http://steck.us/alkalidata/*, 2001.

[23] A. Harter and J. Hecker Denschlag. Cold atom-ion experiments in hybrid traps. *Contemporary Physics*, 55(1):33–45, 2014.

[24] Paul Langevin. Une formule fondamentale de theorie cinetique. *Annales des Chimie et des Physique*, 5:245, 1905.

[25] Ziv Meir, Tomas Sikorsky, Ruti Ben-shlomi, Nitzan Akerman, Meirav Pinkas, Yehonatan Dallal, and Roee Ozeri. Experimental apparatus for overlapping a ground-state cooled ion with ultracold atoms. *Journal of Modern Optics*, 0340(December 2017):1–19, 2017.

[26] D Leibfried, R Blatt, C Monroe, and D Wineland. Quantum dynamics of single trapped ions. *Review of Modern Physics*, 75(1):281–324, 2003.

[27] S. Redner. Random multiplicative processes: An elementary tutorial. *American Journal of Physics*, 58(3):267–273, 1990.

[28] Alexander Lambrecht, Julian Schmidt, Pascal Weckesser, Markus Debatin, Leon Karpa, and Tobias Schaetz. Long lifetimes and effective isolation of ions in optical and electrostatic traps. *Nature Photonics*, 11(11):704–707, 2017.

A EMM estimation

The shelving probability to the excited state when the ion starts in its ground state is given by"

$$p = \sin^2\left(\frac{\pi t}{2t_0}\right)$$

where t_0 is the pi time (maximal shelving probability) and t is pulse time.

From this expression, we can find the π time from the shelving probability for an arbitrary pulse time:

$$t_0 = \frac{t\pi}{2\arcsin\left(\sqrt{p}\right)}$$

The modulation depth of the EMM is given by:

$$\frac{t_{carrier}}{t_{SB}} = \frac{\beta}{2} = \frac{\pi}{\lambda}\cos\theta u_{EMM}$$

where $t_{carrier}$ is the pi time of the carrier transition, t_{SB} is the pi time of the sideband transition, λ is the wavelength,θ is the angle between the laser beam to the radial plane and u_{EMM} is the amplitude of the EMM.

The EMM energy is then[14]:

$$k_B T_{EMM} = \frac{1}{4}m\Omega^2 u_{EMM} = m\Omega^2\left(\frac{t_{carrier}\lambda\arcsin\left(\sqrt{p}\right)}{t\pi^2\cos\theta}\right)^2$$

Hence, the EMM energy after the compensation process can be calculated from the minimal shelving probability.[15]

---

[14] averaged over a single secular cycle

[15] This gives an upper bound to the EMM. The shelving probability can be higher due to other contributions, e.g. temperature (see [25]).

B Beam angles measurements

In order to preform thermometry with Rabi carrier spectroscopy, the angles between the laser beam and the different modes of the ion motion must be measured.

If the ion is ground state cooled, most of the ion population is in $n = 0$ level. Preforming Rabi carrier pulse (on-resonance) will give the following shelving probability:

$$P_{D,Carrier}\left(t_R\right) = \sin^2\left(\Omega_0 t_R\right)$$

In the same way, we can preform Rabi pulses, but now on the blue side-band which will give shelving probability:

$$P_{D,BSB}\left(t_R\right) = \sin^2\left(\Omega_{0,1} t_R\right)$$

Where $\Omega_{0,1}$ is the Rabi frequency of the $|g,0\rangle \to |e,1\rangle$ transition.

In the Lamb-Dicke regime[26]:

$$\Omega_{n,n+1} = \Omega_0\sqrt{n+1}\eta$$

Hence:

$$\frac{\Omega_{0,1}}{\Omega_0} = \eta = \frac{\boldsymbol{k}\cdot\hat{\boldsymbol{x}}}{\sqrt{\frac{\hbar}{2m\omega_i}}} = \sqrt{\frac{2m\omega_i}{\hbar}}\frac{2\pi}{\lambda}\cos\theta$$

$$\Rightarrow \cos\theta_i = \frac{\Omega_{0,1}}{\Omega_0}\frac{\lambda}{2\pi}\sqrt{\frac{\hbar}{2m\omega_i}}$$

Where θ is the angle between the beam to the i-th mode, and $\lambda = 674nm$ is the laser wavelength. Hence by measuring the Rabi frequencies on the carrier and all blue sidebands when the ion is ground-state cooled the angles can be calculated.[16]

---

[16] Actually, it is enough to measure only 3 of the frequencies. Since the modes are orthogonal, the angles satisfy:

$$\cos^2\theta_x + \cos^2\theta_y + \cos^2\theta_x = 1$$